SOURCE DATA · TRANSPARENT PROCESS · OPEN ACCESS

RAB11A and RAB11B control mitotic spindle function in intestinal epithelial progenitor cells

Ivor Joseph[1,†], Juan Flores[1,†], Victoria Farrell[1], Justin Davis[1] (ID), Jared Bianchi-Smak[1], Qiang Feng[1], Sayantani Goswami[1], Xiang Lin[2], Zhi Wei[2], Kevin Tong[3] (ID), Zhaohui Feng[4], Michael P Verzi[3], Edward M Bonder[1], James R Goldenring[5] (ID) & Nan Gao[1,*] (ID)

Abstract

RAB11 small GTPases and associated recycling endosome have been localized to mitotic spindles and implicated in regulating mitosis. However, the physiological significance of such regulation has not been observed in mammalian tissues. We have used newly engineered mouse models to investigate intestinal epithelial renewal in the absence of single or double isoforms of RAB11 family members: Rab11a and Rab11b. Comparing with single knockouts, mice with compound ablation demonstrate a defective cell cycle entry and robust mitotic arrest followed by apoptosis, leading to a total penetrance of lethality within 3 days of gene ablation. Upon *Rab11* deletion *ex vivo*, enteroids show abnormal mitotic spindle formation and cell death. Untargeted proteomic profiling of Rab11a and Rab11b immunoprecipitates has uncovered a shared interactome containing mitotic spindle microtubule regulators. Disrupting Rab11 alters kinesin motor KIF11 function and impairs bipolar spindle formation and cell division. These data demonstrate that RAB11A and RAB11B redundantly control mitotic spindle function and intestinal progenitor cell division, a mechanism that may be utilized to govern the homeostasis and renewal of other mammalian tissues.

Introduction

Transport and distribution of proteins to distinct cellular compartments are essential for eukaryotic cell functions and tissue homeostasis. The Rab family of small GTPases play a crucial role in regulating the vesicular transport of proteins in exocytic or endocytic pathways (Li & Marlin, 2015). Individual Rab family members are tasked with specific sorting or trafficking processes (Martinez & Goud, 1998). These Rab proteins are evolutionarily conserved and their disruptions have been implicated in diseases including, but not limited to, cancer, neurodegeneration, and genetic disorders (Bravo-Cordero *et al*, 2007; Goldenring, 2013; Kajiho *et al*, 2016; Guadagno & Progida, 2019).

RAB11 family members regulate recycling of internalized proteins and trafficking them back to the plasma membrane in nonpolarized and polarized epithelial cells (Green *et al*, 1997; Wang *et al*, 2000; Hales *et al*, 2002). The mammalian RAB11 family has three isoforms, RAB11A, RAB11B, and RAB25 (Bhartur *et al*, 2000; Kumar & Lukman, 2018). RAB11A and RAB11B are 89% identical in amino acid sequence (Bhartur *et al*, 2000; Kumar & Lukman, 2018; Ferro *et al*, 2021), while RAB25 possesses 61% similarity to RAB11A and 66% similarity to RAB11B (Bhartur *et al*, 2000; Kumar & Lukman, 2018). RAB11A was originally isolated from bovine brain tissue (Kikuchi *et al*, 1988; Sakurada *et al*, 1991; Kelly *et al*, 2012) and was later found to be ubiquitously expressed in mammalian cell types (Lapierre *et al*, 2003; Xu *et al*, 2011). RAB11B is enriched in the brain, heart, and testes (Kelly *et al*, 2012) and is also found in polarized intestinal epithelial cells (Silvis *et al*, 2009). RAB25, originally identified in rabbit parietal cells, is expressed mostly in epithelial cells (Goldenring *et al*, 1993; Kelly *et al*, 2012). RAB11A and RAB11B were found localized to the vesicular compartments of recycling endosome and the trans-Golgi network (Goldenring *et al*, 1996; Casanova *et al*, 1999; Welz *et al*, 2014). Collectively, RAB11 isoforms are considered to be responsible for trafficking many transmembrane proteins and lipids to the plasma membrane (Ullrich *et al*, 1996; Maxfield & McGraw, 2004; Ferro *et al*, 2021). For example, RAB11A-dependent trafficking of E-cadherin establishes epithelial cell polarity (Desclozeaux *et al*, 2008; Welz *et al*, 2014). RAB11-mediated trafficking of aquaporin-2 regulates water reabsorption in renal collecting ductal principal cells (Nedvetsky *et al*, 2007). Recycling of CXCR2 through RAB11

---

1 Department of Biological Sciences, Rutgers University, Newark, NJ, USA
2 Department of Computer Sciences, New Jersey Institute of Technology, Newark, NJ, USA
3 Department of Genetics, Rutgers University, New Brunswick, NJ, USA
4 Rutgers Cancer Institute of New Jersey, New Brunswick, NJ, USA
5 Section of Surgical Sciences and Epithelial Biology Center, Vanderbilt University Medical Center, Nashville, TN, USA
*Corresponding author. Tel: +1 973 353 5523; E-mail: ngao@newark.rutgers.edu
†These authors contributed equally to this work

vesicles is critical for physiological response to a chemokine (Fan *et al*, 2004). HeLa cell lines engineered to be devoid of either *RAB11A* or *RAB11B* showed a perturbation of the endosomal-lysosomal pathway (Zulkefli *et al*, 2019). The functional difference or redundancy between RAB11A and RAB11B has not been defined at tissue level in mammals.

RAB-dependent vesicular movement frequently depends on actin or microtubule-based motor proteins (Hammer & Wu, 2002; Horgan & McCaffrey, 2011). Since its isolation through a yeast two-hybrid screening, MYOSIN-Vb has been the most characterized RAB11-interacting motor that complexes through its tail domain with all RAB11 members (Lapierre *et al*, 2001). Protein complexes formed by RAB11A, MYOSIN-Vb, and RAB11-family interacting proteins (FIP) are critical for movement of the recycling vesicles (Hales *et al*, 2002; Wang *et al*, 2008; Schuh, 2011; Schafer *et al*, 2014; Welz *et al*, 2014). Interestingly, endogenous RAB11B was found localized to an apical pericentrisomal region that was distinct from RAB11A localization, and the microtubule agents nocodazole and taxol alter RAB11A's intracellular localization (Lapierre *et al*, 2003).

In *Caenorhabditis elegan*s, RAB11 was previously detected in a screen for regulators of mitotic spindle dynamics and was later found to require Receptor of Activated C Kinase 1 (RACK-1) to redistribute RAB11 recycling endosomes during the cell cycle, and to direct them in a dynactin-dependent mechanism to the pericentrosomal region and spindle (Zhang *et al*, 2008b; Ai *et al*, 2009). RAB11 family interacting protein 3 in complex with RAB11 was required for completion of cytokinesis (Wilson *et al*, 2005), while RNAi-based *Rab11* depletion in *Caenorhabditis elegans* caused abnormal microtubule dynamics and spindle alignment during metaphase (Zhang *et al*, 2008b). In cultured cells, mitotic recycling endosomes were found to bind the gamma-tubulin ring complex (γ-TuRC) components and associate with tubulin *in vitro*. Rab11 depletion or functional disruption perturbed astral microtubules, redistributed spindle pole proteins, and delayed mitosis (Hehnly & Doxsey, 2014). The idea that RAB11 regulates spindle pole maturation during mitosis has not been formally validated *in vivo* such as in mouse models, and the physiological significance of such regulation is unknown at a tissue level.

Previously, we reported that global knockout of Rab11a in mice caused embryonic lethality during implantation stage and that *Rab11a*-null mouse embryonic fibroblasts divided normally (Yu *et al*, 2014b). Mice with intestinal epithelial cell (IEC)-specific knockout of *Rab11a* had mislocalized brush border proteins, increased inflammatory cytokine production, epithelial hyperplasia, and elevated susceptibility to intestinal tumorigenesis (Sobajima *et al*, 2014; Yu *et al*, 2014a; Knowles *et al*, 2015; Feng *et al*, 2017; D'Agostino *et al*, 2019). However, no mitotic spindle defect was observed in *Rab11a*-deficient IECs (Yu *et al*, 2014a). Here, we newly developed mouse models that lack both *Rab11a* and *Rab11b* in the IECs. We found that, unlike *Rab11a* or *Rab11b* single knockouts, the double knockout mice, upon gene ablation, developed rapid spindle defects in the cycling progenitor cells and robust epithelial apoptosis, leading to mortality with full penetrance. Using Rab11a and Rab11b proteomic analysis, we shed lights on their common spindle-associated protein targets, including the microtubule kinesin motor KIF11. We propose that the mammalian RAB11A and RAB11B redundantly regulate mitotic spindle function in tissue progenitor cells to maintain homeostasis.

Results

Ablation of *Rab11a* and *Rab11b* in adult intestinal epithelium disrupts tissue renewal

Using CRISPR-Cas9 genome editing, we developed a *Rab11b* knockout mouse allele, where exons 2, 3, and 4 of *Rab11b* were removed (Fig EV1A–C, please see method). *Rab11b*$^{-/-}$ mice are viable and fertile. The high sequence homology between Rab11a and Rab11b suggested a potential functional redundancy (Lai *et al*, 1994; Silvis *et al*, 2009). We thus developed *Rab11a*$^{Fl/Fl}$; *Rab11b*$^{-/-}$; *Villin-Cre* mice, where *Rab11a* was constitutively deleted in all intestinal epithelial cells (IECs) on a *Rab11b* global knockout background. By breeding *Rab11a*$^{Fl/+}$; *Rab11b*$^{+/-}$; *Villin-Cre* mice to *Rab11a*$^{Fl/Fl}$; *Rab11*$^{-/-}$ mice, we obtained 4% of live pups that were *Rab11a*$^{Fl/Fl}$; *Rab11b*$^{-/-}$; *Villin-Cre* on the date of birth. This ratio was lower than expected Mendelian ratio of 12.5%. All these *Rab11a*$^{Fl/Fl}$; *Rab11b*$^{-/-}$; *Villin-Cre* pups died on the first day of birth (red line, Fig 1A). Fifty percent of *Rab11a*$^{Fl/Fl}$; *Rab11b*$^{+/-}$; *Villin-Cre* mice that had homozygous *Rab11a* deletion but retained a single *Rab11b* copy died prior to postnatal Day 4 (P4), and none survived to 1 week old (green line, Fig 1A). These observations were consistent across multiple breeding pairs. Thus, unlike single gene knockouts, loss of both *Rab11a* and *Rab11b* in the developing IECs led to lethality, suggesting that Rab11a and Rab11b have some redundant functions in contributing to the survival of mice.

To examine the impact of *Rab11a* and *Rab11b* deletion on adult intestinal epithelia, we next used the inducible *Villin-CreER* driver to facilitate gene ablation. Adult *Rab11a*$^{Fl/Fl}$; *Rab11b*$^{-/-}$; *Villin-CreER* mice (also referred to as DKO in some figures) were injected with 1 single dose of tamoxifen to delete *Rab11a* on the *Rab11b*$^{-/-}$ background. Western blots using intestinal lysates showed that, in DKO mice, Rab11a abundance decreased gradually in the first 2 days and diminished on Day 3 following tamoxifen injection (Fig 1B). Upon tamoxifen injection, DKO mice exhibited rapid body weight loss while *Rab11a*$^{Fl/Fl}$; *Rab11b*$^{+/-}$; *Villin-CreER* mice with only one remaining *Rab11b* wild-type copy showed a noticeable body weight loss (Fig EV2A). All DKO mice died on Day 2 or Day 3 after tamoxifen injection. *Rab11a*$^{Fl/Fl}$; *Rab11b*$^{+/-}$; *Villin-CreER* mice died within a week of tamoxifen injection. This lethality phenotype of DKO was observed from different breeding pairs in independent experiments (*n* > 50 mice). Littermates that were deficient for only *Rab11a* or *Rab11b* did not show body weight loss after tamoxifen injection (Fig EV2A). Thus, inducible IEC-specific deletion of *Rab11a* and *Rab11b* in adult mice caused a full penetrance lethality, suggesting that Rab11a and Rab11b redundantly regulate some vital functions that maintain intestinal tissue homeostasis.

Histological examination revealed that the intestinal villi of DKO mice became noticeably blunted on Day 2 and severely flattened on Day 3 after tamoxifen (TAM) injection, at which time point all DKO mice died (Figs 1C and EV2B). Immunofluorescent analysis for the intestinal alkaline phosphatase (AP), an enterocyte marker expressed by differentiated villus epithelium (Fawley & Gourlay, 2016) suggested a significant reduction of enterocytes on Day 3 post-TAM treatment in DKO mice (Fig 1D and E). A similar observation was made by staining for Villin, an enterocyte brush border protein (Fig EV2C). Alcian blue (Fig 1F and G) and lysozyme (Fig 1H and I) staining suggested a decline in total number of goblet
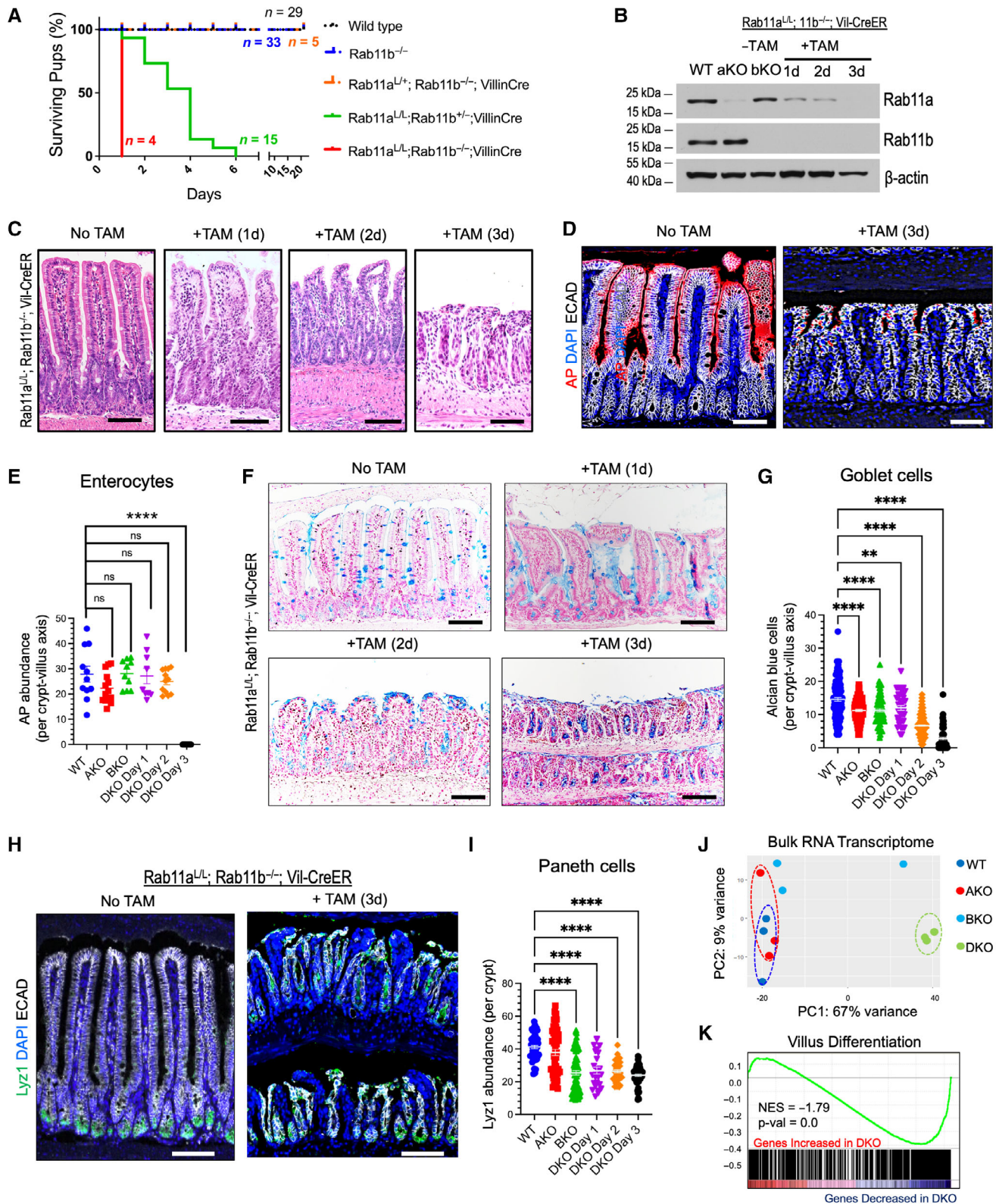
Figure 1.

Figure 1. Ablation of *Rab11a* and *Rab11b* in IEC disrupts intestinal epithelial differentiation and homeostasis.

A Survival graphs of newborn pups from breeding of *Rab11a^{Fl/+}*; *Rab11b^{+/−}*; *Villin-Cre* and *Rab11a^{Fl/+}*; *Rab11b^{+/−}* (or *Rab11a^{Fl/+}*; *Rab11b^{−/−}*) mice. The total number of pups for each genotype was labeled next to the corresponding curve. The graph represents over six independent litters from three different mating pairs.

B Western blots for Rab11a and Rab11b using small intestinal lysates prepared from adult wild-type (WT, lane 1), *Rab11a^{Fl/Fl}*; *Villin-CreER* (aKO, lane 2) 2 days after tamoxifen treatment, *Rab11b^{−/−}* (bKO, lane 3), and *Rab11a^{Fl/Fl}*; *Rab11b^{−/−}*; *Villin-CreER* (DKO) mice 1 day (lane 4), 2 days (lane 5), and 3 days (lane 6) after tamoxifen treatment. All mice were given a single tamoxifen injection. β-actin was used as loading control. Results represent more than three independent experiments.

C H. & E. staining of adult *Rab11a^{Fl/Fl}*; *Rab11b^{−/−}*; *Villin-CreER* mice, before and after tamoxifen injection. Images represent jejunum tissues collected 1, 2, and 3 days following tamoxifen injection. Experiments were repeated over five times using independent litters ($n > 10$). Scale bars, 50 μm.

D Alkaline phosphatase (AP) staining was performed on intestinal tissue sections of adult *Rab11a^{Fl/Fl}*; *Rab11b^{−/−}*; *Villin-CreER* mice that were treated with corn oil or with tamoxifen. Results represent at least three independent experiments. Scale bars, 50 μm.

E Quantification of AP staining in mice of various genotypes. The AP fluorescent signal abundance per crypt-villus axis was quantified by ImageJ. Data represent 5–6 different microscopic fields taken from three mice per condition.

F Alcian blue staining was performed on adult *Rab11a^{Fl/Fl}*; *Rab11b^{−/−}*; *Villin-CreER* mice before or 1–3 days after tamoxifen injection. Results represent at least three independent experiments. Scale bars, 100 μm.

G Quantification of the number of Alcian blue-positive cells per crypt-villus axis in mice of various genotypes. Data represent average values of approximately 10–15 different microscopic fields taken from three mice per condition.

H Immunofluorescent staining for lysozyme and E-Cad was performed on adult *Rab11a^{Fl/Fl}*; *Rab11b^{−/−}*; *Villin-CreER* mice before and after tamoxifen injection. Experiments represent three independent replicates. Scale bars, 50 μm.

I Quantification of lysozyme fluorescent signal abundance per crypt in mice of various genotypes. Data represent approximately 10–15 different microscopic fields taken from three mice per condition.

J Bulk RNA sequencing was performed on WT, aKO, bKO, and DKO mouse jejunum tissues ($n = 3$ each group) 2 days after tamoxifen injection. The resulting transcriptomes were analyzed by principle coordinate analysis.

K Gene set enrichment analysis (GSEA) was performed for villus epithelial differentiation transcriptome to compare WT and DKO mice. This differentiation gene set was significantly reduced in DKO. *P*-value < 0.001.

Data information: One-way Anova was used in Fig 1E, G and I, where error bars represent SEM, and **$P < 0.01$; ****$P < 0.0001$.
Source data are available online for this figure.

and Paneth cells per crypt-villus axis, respectively. Reduction in goblet and Paneth cells became the most pronounced on Day 3 in DKO intestines (Fig 1F and H).

As the DKO mouse intestinal phenotype became obvious on Day 2 after TAM treatment and the majority of them were still alive, we sought to investigating the global transcriptomic changes in these DKO mice on Day 2. We performed a bulk RNA-sequencing analysis on jejunums of Day 2 DKO mice. In the same experiment, we included mice of single Rab11a or Rab11b deficiency, as well as littermate wild-type mice as controls. Principle coordinate analysis (PCA) of transcriptomes showed that DKO mice were clustered away from all other groups (green, Fig 1J). Gene set enrichment analysis (GSEA) confirmed that there was a significant loss of villus epithelial differentiation transcriptome in DKO intestines ($P < 0.001$, Fig 1K).

Rab11a and Rab11b DKO mice have an impaired intestinal stem cell and proliferative capacity

To examine whether a loss of epithelial proliferation may have contributed to the rapid villus blunting in DKO mice, we assessed the signature gene set for epithelial cell proliferation. Surprisingly, Day 2 DKO intestines had a significantly enriched transcriptome for proliferation (Fig 2A). Indeed, 2 days after TAM, Ki67+ IECs (Figs 2B and C, and EV2D) and pHH3+ mitotic cells (Fig 2D and E) were both increased in DKO intestinal epithelia. However, their numbers reduced on Day 3 (Fig 2C and E), indicating a transient hyperproliferative state followed by a possible loss of the proliferative compartment.

Investigating signature genes for intestinal stem cells (ISCs) revealed that DKO mice had decreased transcripts of the fast-cycling stem cells, such as *Olfm4*, *Ascl2*, and *Lgr5* (Fig 2F). However, abundances of *Sox9*, *Bmi1*, *Hopx*, and *Lrig1* were elevated (Fig 2F). Western blot (Fig 2G) and staining for Olfm4 validated this reduction of crypt base columnar ISCs following *Rab11* ablation (Fig 2H and I). In contrast, the mitotic marker pHH3 was elevated at Day 2 (Fig 2G), and the number of Sox9+ crypt IECs was increased in DKO (Fig 2J and K). In addition, staining for c-Myc, which marks the transit-amplifying IECs (Bettess *et al*, 2005), revealed a marked expansion in DKO mice starting from the first day after *Rab11a* ablation (Fig 2L and M). Mice losing single *Rab11a* or *Rab11b* did not exhibit significant alterations in these markers, suggesting that Rab11a and Rab11b redundantly regulate the intestinal tissue maintenance in adult mice.

Loss of Rab11a and Rab11b causes cell cycle arrest

To determine the cell cycle distribution of the IECs in DKO mice, we performed flow cytometry analysis on single IEC suspensions prepared from DKO mice 2 days after tamoxifen treatment and stained by propidium iodide. Comparing with WT IECs, DKO cells exhibited a 4.4-fold increase in percentage of cells in G2/M phase and 2.9-fold increase in S-phase cells (Fig 3A and B). The flow cytometry also suggested more apoptotic IECs in DKO mice than in WT mice.

To investigate whether there was a cell cycle blockage or an overall cell cycle redistribution, we performed CIdU/IdU pulse-chase labeling experiments. DKO mice and WT littermates (no Cre) were first injected with tamoxifen. Twenty-four hours later, mice were injected with CIdU to label S-phase cells (Fig 3C). Mice were sacrificed after 24–36 h, each receiving an injection of IdU 3 h before the sacrifice. Intestinal sections were stained for CIdU (green) and IdU (red) (Fig 3D). CIdU-labeled WT cells were able to make to the upper villus region, while DKO cells remained in the crypt or lower villus region (Fig 3D). Compared with WT mice, DKO mice had a significant increase in the number of CldU+/IdU+ double-positive cells (Fig 3D and E) and IdU+ cells (Fig 3F and G), indicating increased cycling cells on Day 2 as well as a delay of cell cycle transition by DKO cells. We also noticed a significantly increased

number of CIdU⁺ DKO cells that were shedding off the epithelial lining (pointed by arrows in Fig 3D, F and H), indicating that some DKO cells went into cell cycle and died. These data collectively suggested that there was an increased cell cycle entry as well as a cell cycle arrest of DKO cells, which were associated with a loss of these cycling cells.

Rab11a and Rab11b co-immunoprecipitate with mitotic spindle proteins

The above results suggest that Rab11a and Rab11b redundantly regulate cell division. To biochemically profile potential common protein networks of Rab11a and Rab11b, we performed proteomic
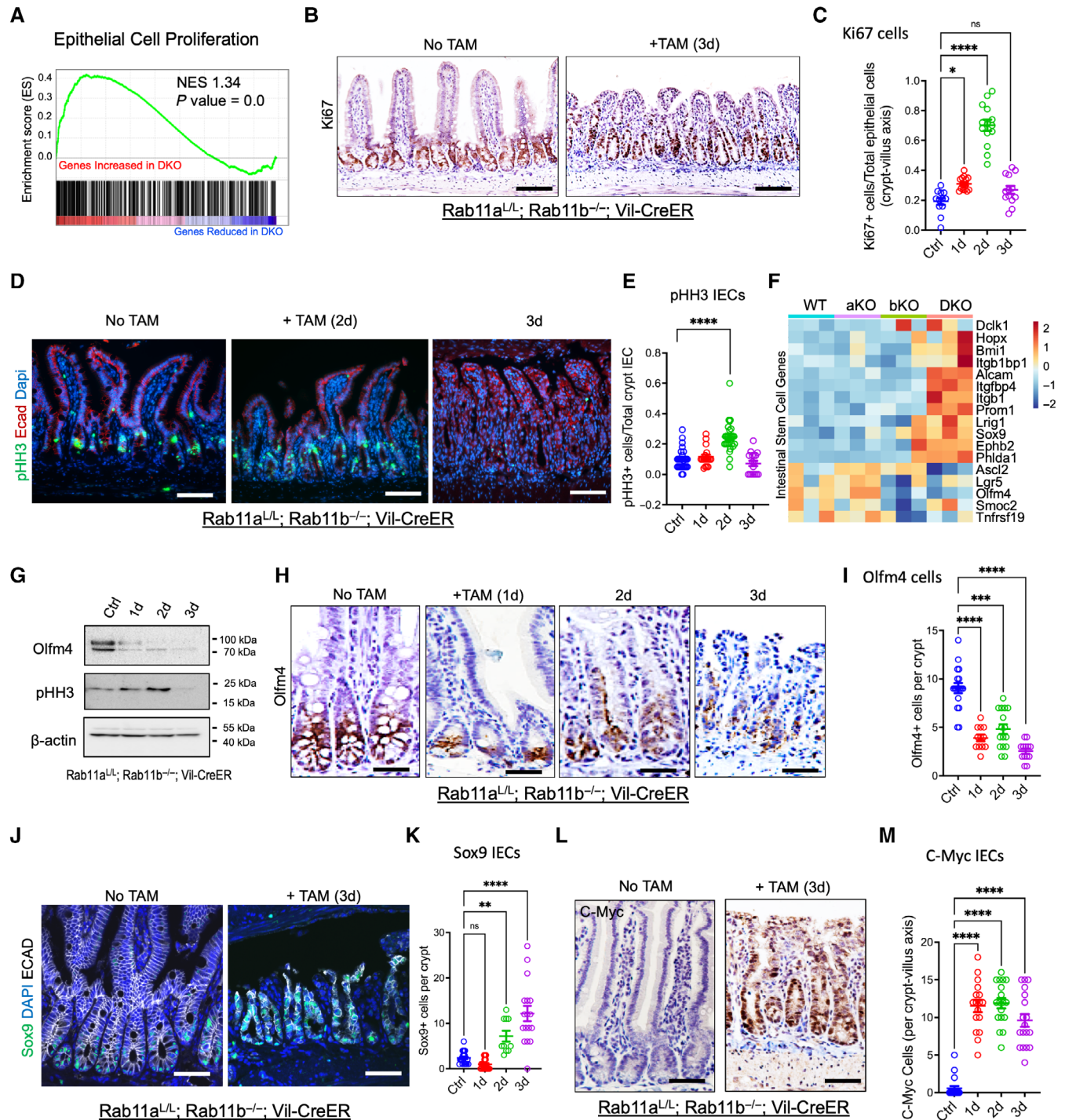

Figure 2.

◀

Figure 2. DKO mice show impaired tissue renewal and proliferation.

A   GSEA analysis shows increased epithelial cell proliferation gene sets in DKO mice.

B   Immunohistochemistry for Ki67 staining was performed on intestinal sections of adult *Rab11a*$^{Fl/Fl}$; *Rab11b*$^{-/-}$; *Villin-CreER* mice before and after tamoxifen injection. Experiments represent three independent replicates. Scale bars, 50 μm.

C   Quantification of ratio of Ki67$^+$ cells over total epithelial cells per crypt-villus axis in DKO mice before and after tamoxifen treatment. Data represent approximately 10–15 different microscopic fields taken from three mice per condition.

D   Immunofluorescent staining for pHH3 and E-Cad was performed on intestinal sections of adult *Rab11a*$^{Fl/Fl}$; *Rab11b*$^{-/-}$; *Villin-CreER* mice before and after tamoxifen injection. Experiments represent three independent replicates. Scale bars, 50 μm.

E   Quantification of ratio of pHH3$^+$ cells over total IECs per crypt in DKO mice before and after tamoxifen treatment. Data represent approximately 10–15 different microscopic fields taken from three mice per condition.

F   Heat maps of intestinal stem cell signature genes of mice of various genotypes.

G   Representative western blots for Olfm4 and pHH3 in intestinal tissue lysates of DKO mice before and after tamoxifen injection.

H   Immunohistochemistry for Olfm4 was performed on intestinal sections of adult *Rab11a*$^{Fl/Fl}$; *Rab11b*$^{-/-}$; *Villin-CreER* mice before and after tamoxifen injection. Experiments represent three independent replicates. Scale bars, 50 μm.

I   Quantification of Olfm4$^+$ cell number per crypt in DKO mice before and after tamoxifen treatment. Data represent approximately 10–15 different microscopic fields taken from three mice per condition.

J   Immunofluorescent staining for Sox9 and E-Cad in DKO mice before and after tamoxifen treatment. Scale bars, 50 μm.

K   Quantification of Sox9$^+$ cell number per crypt in DKO mice before and after tamoxifen treatment. Data represent approximately 10–15 different microscopic fields taken from three mice per condition.

L   Immunohistochemistry for c-Myc was performed on intestinal sections of adult *Rab11a*$^{Fl/Fl}$; *Rab11b*$^{-/-}$; *Villin-CreER* mice before and after tamoxifen injection. Experiments represent three independent replicates. Scale bars, 50 μm.

M   Quantification of c-Myc$^+$ cell number per crypt-villus axis in DKO mice before and after tamoxifen treatment. Data represent approximately 10–15 different microscopic fields taken from three mice per condition.

Data information: One-way Anova was performed for Fig 2C, E, I, K and M, where error bars represent SEM. and *$P < 0.05$; **$P < 0.01$; ***$P < 0.001$; ****$P < 0.0001$.
Source data are available online for this figure.

analyses using mass spectrometry on 3× Flag-tagged Rab11a or Rab11b co-immunoprecipitated (co-IP) from HEK293 cells (Fig 4A). This untargeted assay was not purposed for identifying direct binding partners, but rather to globally profile large protein complexes that may be pulled down with either Rab11a or Rab11b. Eight hundred and eighty-five proteins were detected to be shared by Rab11a and Rab11b precipitates (Fig 4B), constituting 93% of Rab11a's total proteomics (Fig 4C). Gene Ontology analysis of these common proteins suggested enriched protein networks for DNA replication (*P*-value = 1.6e-7), cell cycle (*P*-value = 1.7e-5), and mitosis (*P*-value = 1.2e-3; Fig 4D). We ranked the shared targets by their proteomic spectrum counts and uncovered the top 10 proteins: KIF11, MYH9, HSP90AB1, FLNA, HSPA5, FASN, ENO1, NCL, MYH10, and RAB11FIP1. Among them, RAB11FIP1 is a well-known RAB11-interacting protein (Hales *et al*, 2001; Jin & Goldenring, 2006; Baetz & Goldenring, 2013), while KIF11, MYH9, and MYH10 are all myosin or kinesin motor proteins (Fig 4E).

Our proteomic results revealed 37 unique KIF11 peptides in Rab11a precipitates and 20 unique peptides in Rab11b precipitates (Fig EV3A). KIF11 is known to form cross-bridges between pairs of oppositely oriented spindle microtubules in prophase and prometaphase, driving apart the duplicated centrosomes during mitotic spindle formation (Kashina *et al*, 1996; Sharp *et al*, 1999). We performed co-IP analysis and consistently verified co-immunoprecipitation of endogenous KIF11 with FLAG-tagged Rab11a or Rab11b, respectively (Fig 4F). Confocal analysis of KIF11 (gray) and mCherry-tagged WT Rab11a (red) illustrated potential association around the spindle poles defined by pericentrin (green) (Fig 4G). At the spindle poles, Pearson's correlation between Rab11a and KIF11 is 0.66 ± 0.05. Localization of Rab11, Rab11-FIP3, and recycling endosome to the spindle pole has been previously described in multiple studies (Zhang *et al*, 2008b; Ai *et al*, 2009; Hehnly & Doxsey, 2014). Consistent with previous reports, overexpressing a dominant negative Rab11a-S25N impaired

normal bipolar spindle formation in approximately 40% of cells (Fig 4G and H). Twenty-eight percent of Rab11a-S25N transfected mitotic cells had monopolar spindles, and 9% had tripolar or multipolar spindle phenotypes (Figs 4G and EV3B). At the spindle pole, Pearson's correlation between Rab11a-S25N and KIF11 is 0.52 ± 0.07. Cells transfected with Rab11a-S20V showed both the presence of bipolar spindles and Rab11a-S20V localization at the spindle poles (Figs 4G and H, and EV3C).

We examined live dividing HEK293 cells labeled by SiR-Tubulin probe to visualize the real-time movement of mitotic spindles. Cells were transiently transfected with WT Rab11a, or Rab11a-S25N, or Rab11a-S20V, all of which were mCherry-tagged. In cells expressing WT Rab11a, a fraction of Rab11a was localized at the mitotic spindle poles, in addition to cytoplasmic localizations. In cells expressing Rab11a-S25N and exhibiting defective spindle, there was a reduced Rab11a-S25N localization at the spindle poles whereas cells expressing Rab11a-S20V showed Rab11a at the mitotic spindle poles (Fig EV4A). There was no difference in the percentage of mitotic cells observed among the different constructs transfected (Fig EV4B), suggesting disrupting Rab11 did not prevent cells entering mitosis. Interphase cells showed WT Rab11a localization surrounding the centrosome (Fig EV4C). Intensity plots of tubulin and Rab11a showed a dip in Rab11a intensity coinciding with the peak of tubulin core (Fig EV4F). This correlation between Rab11a and tubulin was lost in some cells transfected with Rab11a-S25N (Figs EV4D and 4G). Some Rab11a-S20V cells showed restored Rab11a localization around the centrosome (Figs EV4E and 4H). These results confirmed previous studies that disrupting RAB11 function impaired mitotic spindle in cultured cells (Hehnly & Doxsey, 2014).

However, no prior study has examined the *in vivo* impact of Rab11a and Rab11b loss-of-function on Kif11-associated spindle dynamics. We therefore investigated Kif11-associated spindles in Rab11 DKO and wild-type intestines using confocal

immunofluorescent analysis. Over 80% mitotic spindles in WT intestinal crypt IECs are normal bipolar spindles. In contrast, DKO mitotic IECs showed more than 70% abnormal spindles, with the vast majority being monopolar spindles that shifted toward one side of the cells (Figs 4I–K, L and M, and EV5A). Bipolar but tilted spindles were also observed (Fig 4I). IdU labeling of mice suggested that DKO cells with these defective spindles went into cell cycle previously (Figs 4J and EV5B). In all cases of abnormal spindles in DKO, Kif11 remained to associate with the spindle poles marked by either γ-tubulin (Fig 4L) or pericentrin (Fig 4M). These observations
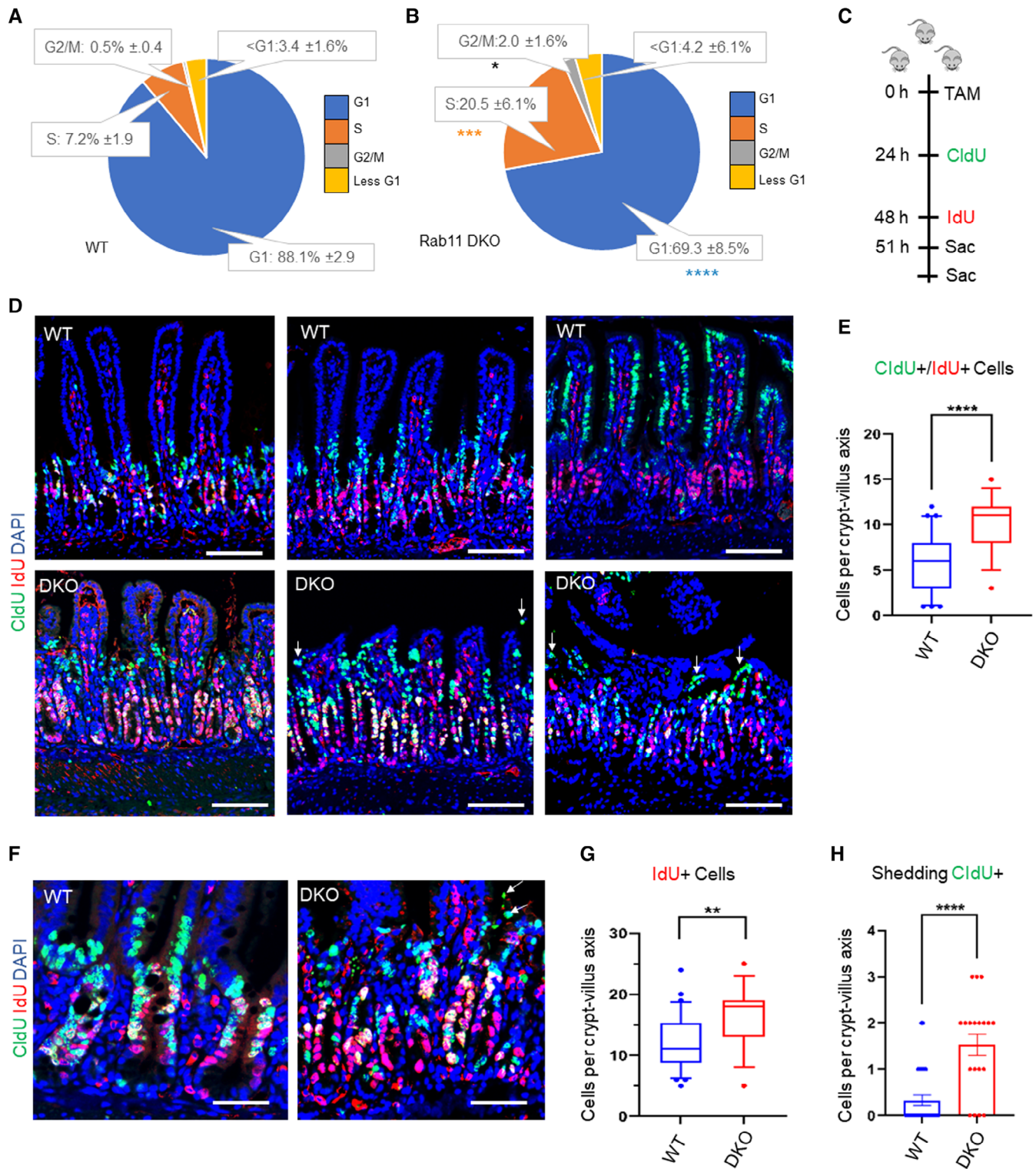

Figure 3.

Figure 3. Loss of *Rab11a* and *Rab11b* in IEC causes cell cycle arrest.

A, B   Jejunum epithelial cells were prepared as single-cell suspension from WT and DKO mice 2 days after tamoxifen injection, stained with propidium iodide, and analyzed for cell cycle distribution by flow cytometry. Pie graphs represent five mice for each genotype in two independent experiments. There was a S-phase ($P < 0.001$) and G2/M phase arrest ($P < 0.05$) in DKO, compared with WT.

C   A schematic diagram shows the sequential CldU and IdU pulse-chase labeling experiments. WT and DKO mice were injected with tamoxifen, first injected by CldU (green) to label S-phase WT and DKO cells; the mice were sacrificed in pairs 1–1.5 days later, with each mouse receiving an IdU (red) injection 3 h before sacrifice to label new dividing cells.

D   Immunofluorescent staining for CldU (green) and IdU (red) in WT and DKO mouse small intestines. An upwards movement of CldU cells was present in WT but not in DKO mice. White arrows point to CldU⁺ DKO epithelial cells that were shedding off the villus surface. Scale bars, 50 μm.

E   Quantification of CldU⁺/IdU⁺ cell number per crypt-villus axis. Data represent 10–15 different microscopic fields taken from three mice per condition.

F   High magnification images were taken from CldU/IdU labeled WT and DKO mouse crypt regions to visualize double-positive cells. White arrows point to shedding CldU cells. Scale bars, 50 μm.

G, H   Quantification of IdU⁺ cells, and shedding CldU⁺ cells per crypt-villus axis in WT and DKO mice. Data represent 10–15 different microscopic fields taken from three mice per condition.

Data information: Welch's *t*-test was used in Fig 3E, G and H. The central band is the median, the boxes represent 25 and 75 percentiles, and the whiskers represent 10 and 90 percentiles. The error bars represent SEM in 3H. **$P < 0.01$; ****$P < 0.0001$.

Source data are available online for this figure.

Disrupting RAB11 biochemically perturbs Kif11-associated protein network

KIF11 forms homo-tetramers via the stalk domain, uses its motor domain to bind microtubules, and hydrolyzes ATP, driving apart the anti-parallel oriented microtubules (Kashina *et al*, 1997). Loss of KIF11 causes mitotic failure (Mayer *et al*, 1999; Bannigan *et al*, 2007). We constructed three truncated KIF11 fragments corresponding to the motor, stalk, and tail domains and tagged them by a V5 epitope (Fig 5A). We overexpressed individual fragments in HEK293T cells and assessed their association with Rab11. Co-IP analysis revealed that the KIF11 stalk region (a.a. 387–861) could associate with both Rab11a (Fig 5B) and Rab11b (Fig 5C). Interestingly, cells overexpressing the stalk region showed an increased frequency of monopolar spindles when compared to cells overexpressing the motor domain (Fig 5D; Appendix Fig S1A). As Kif11 stalk region contains coiled-coil interaction motif that is often used by Rab11 FIP proteins to interact with Rab11 (Wei *et al*, 2006; Lall *et al*, 2015; Kearney & Khan, 2020), we *in vitro* translated Kif11 fragments and tested their binding to purified Rab11 recombinant proteins in buffer. In the conditions tested in our assays, we did not detect a direct KIF11-Rab11 interaction (Appendix Fig S1B and C), suggesting that the observed intracellular KIF11-Rab11 co-precipitation was likely mediated by common interactors.

There are well-characterized KIF11 inhibitors that bind allosteric pockets of KIF11 and inhibit the release of ADP (Yokoyama *et al*, 2018) (Mayer *et al*, 1999; Tcherniuk *et al*, 2010; Venere *et al*, 2015; Wu *et al*, 2018). Previous studies reported a tighter KIF11-association by S-trityl-L-cysteine (STLC) than monastrol (Skoufias *et al*, 2006), and a better pocket-fitting by ispinesib than monastrol (Zhang *et al*, 2008a). We found that cells treated with monastrol (50 μM), S-trityl-L-cysteine (STLC) (2.5 μM), or ispinesib (100 nM), exhibited pronounced monopolar spindle defects (Fig 5E), with STLC and ispinesib eliciting 100% spindle defects (Appendix Fig S1D). RAB11-KIF11 co-precipitation was reduced in all inhibitor-treated cells, while ispinesib caused the greatest reduction (Fig 5F and G). Nocodazole that depolymerizes microtubules also perturbs Rab11-

FIP3 spindle localization (Hehnly & Doxsey, 2014). We found that RAB11-KIF11 association also slightly reduced in cells treated with nocodazole (Fig 5H), collectively suggesting that Rab11 endosomes likely interface with spindle microtubule protein complexes. In all these cases, there were residual intracellular KIF11-RAB11 associations.

We next biochemically examined to what extent depletion of Rab11 might perturb KIF11-associated protein networks. We validated an anti-KIF11 antibody for immunoprecipitation assays (Appendix Fig S1C), pulled down endogenous KIF11 from WT or RAB11-KD Caco2 cells, and subjected the precipitates to an untargeted proteomic analysis by mass spectrometry (Fig 5I). Negative control proteomics from "no antibody" reaction was used to subtract nonspecific background targets. The assay was not purposed for identifying direct KIF11 interactors but for profiling large protein complexes that could be pulled down with KIF11. Two hundred and forty-four targets (25%) present in WT cells were absent in RAB11-KD cells (Fig 5J). String analysis suggested that these proteins play roles in mitosis, DNA replication, and cell cycle progression (Fig 5K). The top 50 affected KIF11-interacting proteins included CLIP1, ZW10, CCAR1, USO1 (p115), CDK9, IQGAP2, SHTN1, and DNM2 (Appendix Fig S2A), which have been associated with mitosis, spindle formation, microtubule, or kinetochore functions (Williams *et al*, 2003; Busch *et al*, 2004; Lopes *et al*, 2005; Vallee *et al*, 2006; Radulescu *et al*, 2011; Lu & Johnston, 2013; Muthu *et al*, 2015). CLIP1 is a plus-end microtubule-binding protein that promotes microtubule growth and microtubule bundling (Komarova *et al*, 2002; Arnal *et al*, 2004; Folker *et al*, 2005). USO1(p115) interacts with γ-tubulin and functions in centrosomal targeting during mitosis (Radulescu *et al*, 2011). CCAR1 interacts with APC-2, a component of the anaphase-promoting complex that drives completion of mitotic cell division (Muthu *et al*, 2015). ZW10 is a kinetochore protein regulating proper chromosome segregation during mitotic division (Starr *et al*, 1997; Jiang *et al*, 2014). We used co-IP analysis and validated a reduced KIF11 association with CLIP1, ZW10, and CCAR1, and to a less extent with USO1(p115) (Fig 5L).

CLIP1 colocalizes with a subset of transferrin receptor-positive endocytic vesicles and links them to microtubules (Pierre *et al*, 1992). As KIF11-CLIP1 co-precipitation was affected by RAB11 deficiency (Fig 5M), we further validated, using confocal immunofluorescent analysis of Kif11 and Clip1 in WT and Rab11 DKO intestinal tissues.

We observed a high colocalization of endogenous Kif11 and Clip1 in WT tissues (Fig 5N), and such correlation was reduced in DKO tissues (Fig 5N and O).

CDK1/cyclin B phosphorylates KIF11 at its tail domain (Blangy et al, 1997) and increases its binding to microtubules in vitro and in Xenopus egg extract spindles (Cahu et al, 2008). Interestingly,
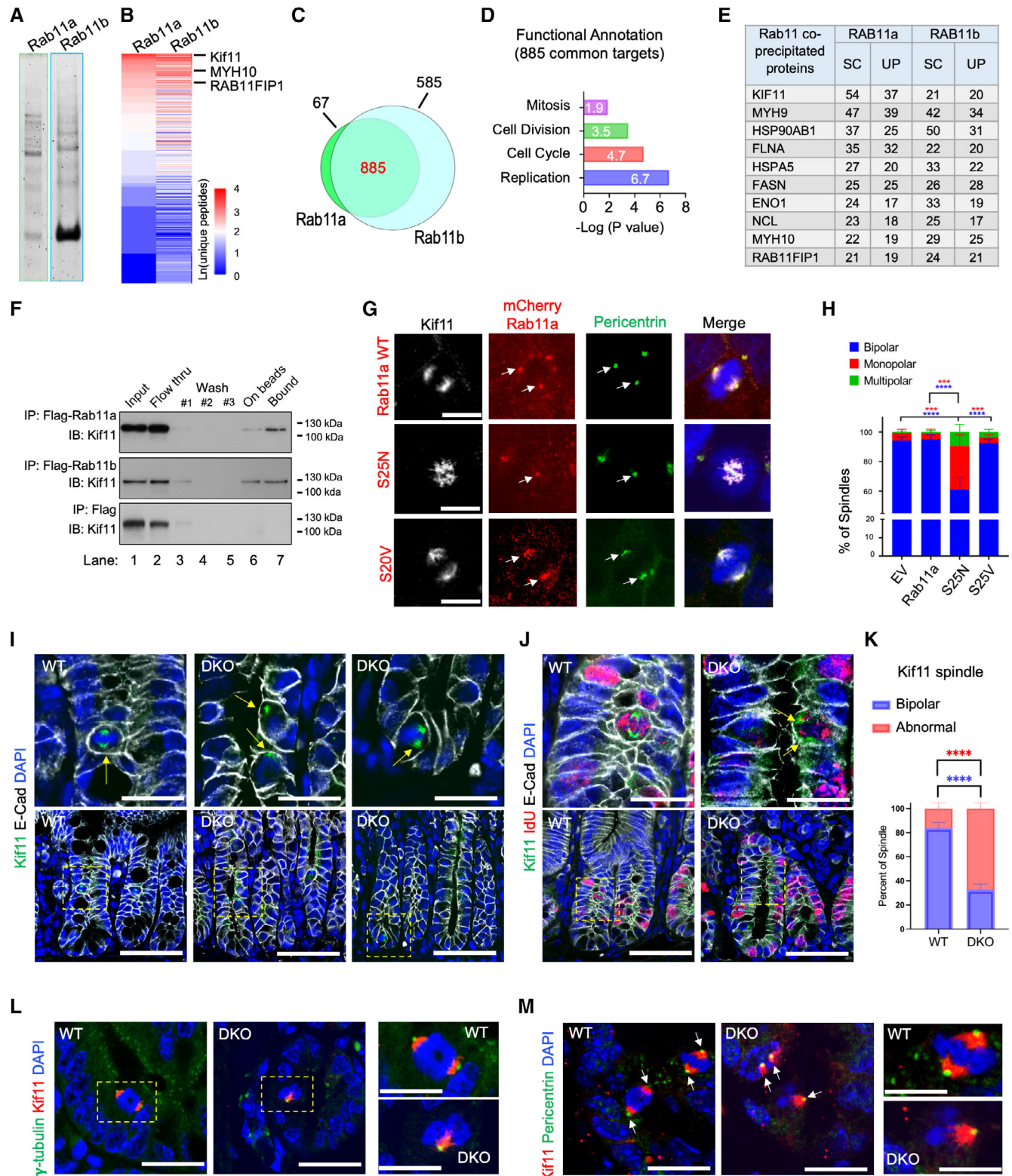

Figure 4.

◄ **Figure 4. Rab11a and Rab11b associate with spindle protein network and redundantly control spindle formation.**

A   HEK293T cells were transfected with 3 × Flag-Rab11a and 3 × Flag-Rab11b, respectively. Immunoprecipitation was performed by using anti-Flag antibody, and the precipitates were resolved on SDS–PAGE, stained by ruby red, and subjected to untargeted proteomic analysis.

B   Heat maps based on unique peptides of protein targets identified by mass spectrometry in 3 × Flag-Rab11a (952 proteins) and 3 × Flag-Rab11b (1,470 proteins) immunoprecipitates. The data were transformed by natural log. Targets with high numbers of unique peptide counts, KIF11, MYH10, and Rab11FIP1, are denoted.

C   Venn diagram shows that 885 protein targets were shared by Rab11a and Rab11b. Note, the majority came down in complexes and may not be direct interactors due to the methods used.

D   Gene Ontology analysis of Rab11a and Rab11b common targets revealed enriched functional networks in DNA replication ($P = 1.6 \times 10^{-7}$), cell cycle ($P = 1.7 \times 10^{-5}$), cell division ($P = 3 \times 10^{-4}$), and mitosis ($P = 1.2 \times 10^{-3}$).

E   The top 10 shared targets ranked by number of spectrum counts (SC) from high to low. Unique peptide (UP) numbers are also provided for each target.

F   Co-IP assays were performed in HEK293T cells to validate the association between 3 × Flag-Rab11a, 3 × Flag-Rab11b and endogenous KIF11. Lane 1: input lysate; lane 2: flow-through after co-IP; lane 3–5: 3 washes; lane 6: on beads; and lane 7: immunoprecipitation elutes. Cells transfected with 3 × Flag empty vector were used as a negative control. Experiments repeated over six times.

G   Cells were transfected with mCherry-tagged WT, Rab11-S25N, and Rab11-S20V, fixed and stained for endogenous KIF11 (gray) and pericentrin (green). The mCherry signal (red) represents direct fluorescent signal visualized under confocal microscope. Arrows denote position of spindle poles defined by pericentrin. Images represent three independent experiments. Scale bars, 10 μm.

H   Quantification of the percentage of bipolar, monopolar, or multipolar (three or more) spindles observed in mitotic cells identified from each microscopic field. Data represent 10–20 independent fields per condition from three experiments.

I   Immunofluorescent staining for KIf11 (green) and E-Cad (gray) in WT and DKO mouse intestines. Yellow arrows point to Kif11$^+$ spindles. Images represent at least 10 images per mouse and five mice for each genotype. Scale bars, 50 μm.

J   WT and DKO mice were injected with IdU 3 h before sacrifice to label new dividing cells. Immunofluorescent staining for KIf11 (green), E-Cad (gray), and IdU (red) was performed. Yellow arrows point to abnormal Kif11 localization in DKO cells. Scale bars, 50 μm.

K   Based on Kif11 spindle morphology, quantification of the percentage of bipolar and abnormal (monopolar, tilted bipolar) spindles was done on WT and DKO intestinal sections. Results were quantified from mitotic cells of 20 independent fields of 5–6 mice for each genotype.

L, M   Immunofluorescent staining for KIf11 (red) and spindle pole markers γ-tubulin or pericentrin (green) in WT and DKO mouse intestines. Images represent three mice for each genotype. White arrows point to spindle pole. Scale bars, 20 μm, 10 μm.

Data information: Two-way Anova was used in Fig 4H and K, where error bars represent SEM, and ***$P < 0.001$; ****$P < 0.0001$.
Source data are available online for this figure.

we detected an increased KIF11-Cyclin B association in RAB11-KD cells compared with WT cells (Fig 5L). We then tested whether mitotic arrest induced by RAB11 deficiency might be correlated with such increased KIF11-Cyclin B association. We treated WT cells with nocodazole to induce a mitotic arrest and found that nocodazole-treated cells had a similarly increased KIF11-Cyclin B association (Appendix Fig S2B). DKO cells with defective mitotic Kif11 spindles also showed elevated Cyclin B1 (Appendix Fig S2C and D). These results suggest that loss of RAB11 led to mitotic defects and impaired KIF11-associated spindle microtubule functions.

Loss of Rab11a and Rab11b in IECs triggers cell-autonomous activation of apoptosis

The robust *in vivo* intestinal phenotype of DKO mice could alternatively be caused by loss of epithelial differentiation or by nonepithelial autonomous mechanisms. We thus grew enteroids from WT and Rab11 single and double knockout mice and treated mature enteroids with 4-OHT to induce Rab11 deletion. Tamoxifen-treated WT or single-knockout enteroids continue to grow, while DKO enteroids became smaller and darker with the cells of the edge starting to deteriorate from Day 2 after treatment (Fig 6A). Five days after treatment, DKO enteroids were further impaired, and propidium iodide (PI) staining showed massive cell death per enteroid quantified by the percentage of PI-stained area (Fig 6B and C). Histological sections confirmed the significantly increased events of impaired DKO enteroids (Fig 6D and E). Confocal immunofluorescent analysis could rarely detect any normal Kif11-positive bipolar spindles in DKO enteroids, while bipolar spindles were seen, with the average frequency of 1 per enteroid,

in WT and single-knockout enteroids, which were also treated with tamoxifen (Fig 6F). Rab11a$^{L/L}$; Rab11b$^{-/-}$; Vil-CreER enteroids treated with vehicle retained normal Kif11-positive bipolar spindles (Fig 6G and H), suggesting simultaneous loss of both Rab11a and Rab11b disrupt bipolar spindle formation. DKO enteroids also contained significantly less pHH3 cells, the death of which could be visible in areas with disintegrating epithelial lining, and pHH3 immunoreactivity was robustly present in the lumen of these impaired DKO enteroids (Fig 6I–K). Furthermore, differentiated Paneth cells could still be detected in the impaired DKO enteroids (Fig 6J and L), collectively suggesting that the observed cell death was caused by IEC autonomous division defect rather than a lack of differentiated cells.

Quantification of cleaved caspase 3 (CC3)-positive IECs showed significantly increased apoptotic cells in the epithelial lining of DKO enteroids (Fig 7A and B), suggesting that an apoptotic program was triggered in the DKO enteroids. Indeed, gene set enrichment analysis revealed a significantly increased apoptotic gene program in Rab11 DKO intestines (Fig 7C and D). Pro-apoptotic genes, including Anax1 (Fig 7E), Anax5 (Fig 7F), Bcl21L (Fig 7G), and Bcl10 (Fig 7H), were robustly increased in DKO intestines compared with WT or single knockouts. DKO intestines contained progressively increased CC3$^+$ apoptotic cells on Day 2 and 3 post-TAM treatment (Fig 7I and J). The major inflammatory driver, TNF and TNFα-NFκB signaling pathway genes were significantly activated in DKO intestines (Fig 7K–M). Immunohistochemistry confirmed a significantly elevated NFκB as the pathway readout in DKO tissues (Fig 7N and O). In addition, p53$^+$ cells were readily detected in DKO intestinal epithelia (Fig 7P; Appendix Fig S2E), consistent with an increased apoptotic response to the genomic stresses triggered by the mitotic spindle checkpoint.

Discussion

By using mouse genetics, we demonstrated here that Rab11a and Rab11b redundantly regulate mitotic spindle function in dividing intestinal epithelial cells. Loss of either Rab11a or Rab11b alone did not cause mitotic defects; however, loss of both disrupted cell division, leading to epithelial cell death and lethality of the animals. Such redundancy in regulating tissue renewal and homeostasis has
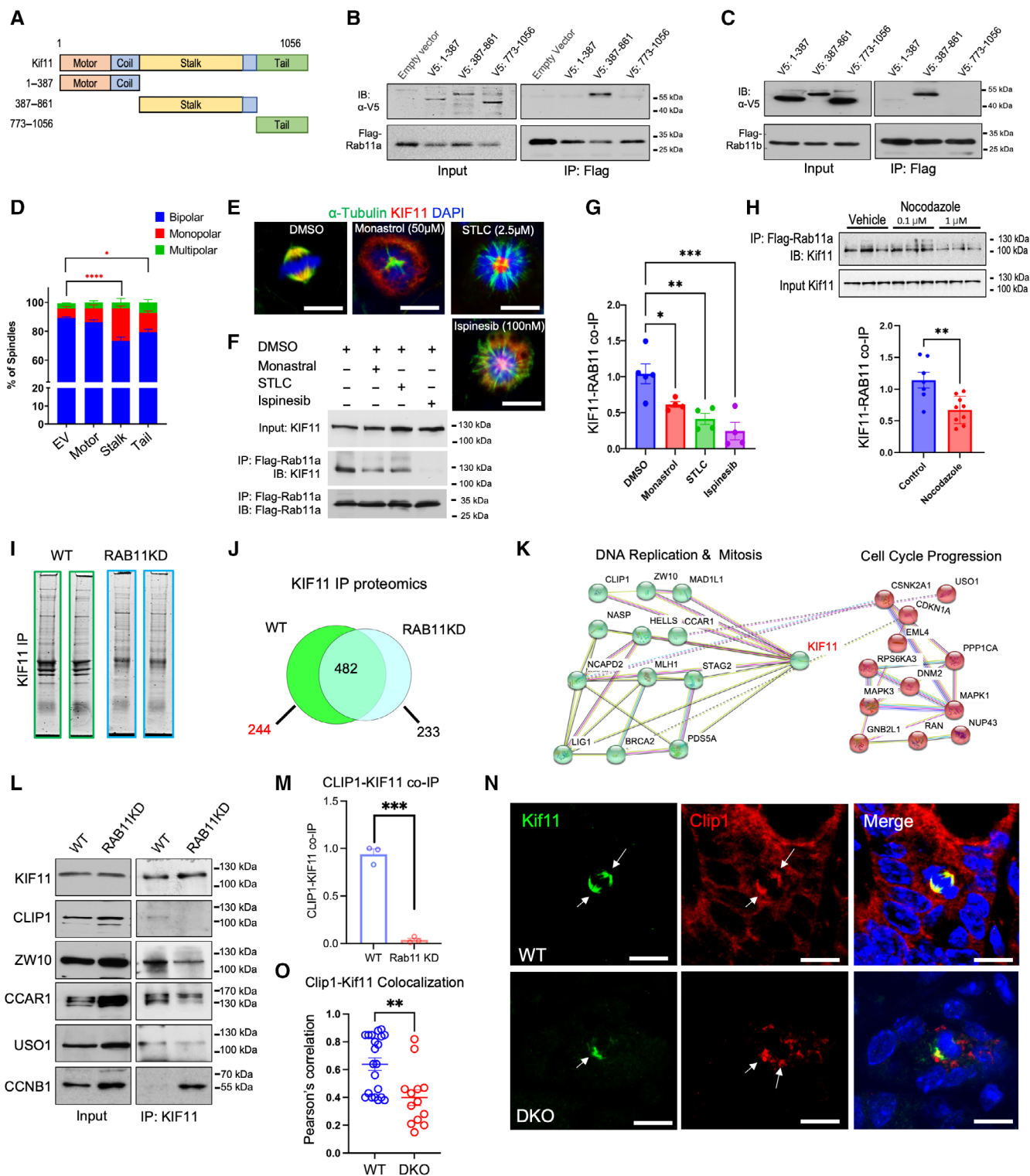

Figure 5.

Figure 5. Deficiency of Rab11a and Rab11b perturbs spindle protein network.

A   A schematic diagram of full length and three truncated KIF11 that represent the motor, the stalk, and the tail domains. All fragments were tagged by a V5 epitope. The corresponding amino acids of each fragment are labeled on the left.

B, C   HEK293T cells were transiently transfected with 3 × Flag-Rab11a (or 3 × Flag-Rab11b) and V5-tagged KIF11 truncates. Lysates were immunoprecipitated by anti-Flag antibody and probed by an anti-V5 antibody to assess intracellular associations. Cells transfected by V5 empty vector were used as a negative control.

D   HEK293T cells were transiently transfected with V5-tagged KIF11 truncates or empty vector, fixed, and stained for KIF11. Percentage of bipolar, monopolar, and multipolar spindles were scored from total mitotic cells identified from each field. Independent fields of three biological replicates per condition were analyzed and represented as stacking bar graphs.

E   Immunofluorescent staining for α-Tubulin and KIF11 was performed on HEK293T cells treated with 0.1% DMSO (as a control), 50 μM monastrol, 2.5 μM STLC, or 100 nM ispinesib. Experiments were done three times. Scale bars, 10 μm.

F   Co-IP assays for 3 × Flag-Rab11a and endogenous KIF11 were performed using HEK293T cells treated with various KIF11 inhibitors. Cells treated with DMSO were used as a control. Anti-Flag precipitates were probed by anti-KIF11 and anti-Flag antibodies.

G   Quantification of co-immunoprecipitated KIF11 was normalized to input KIF11 from cells treated by different inhibitors. DMSO data were quantified for five experimental replicates, and all other treatments were quantified for four experimental replicates.

H   HEK293T cells were transiently transfected with 3 × Flag-Rab11a and treated with nocodazole (100 ng/ml) or vehicle overnight, and lysates were used for Flag immunoprecipitation followed by immunoblot for KIF11. Quantification of co-immunoprecipitated KIF11 was normalized to input KIF11 from control ($n = 6$) and nocodazole-treated ($n = 9$) cells.

I   Endogenous KIF11 was immunoprecipitated from WT and RAB11-knockdown (KD) Caco2 cells. The precipitates were resolved on SDS–PAGE, stained by ruby red, and subjected to an untargeted proteomic analysis.

J   Venn diagram showing that targets (244) in KIF11 precipitates of WT cells were absent from RAB11-KD cells.

K   STRING analysis of KIF11 co-precipitated targets involved in DNA replication, mitosis, and cell cycle regulation.

L   KIF11 co-IP analysis was performed using WT and RAB11-KD CaCo2 cell lysates. The immunoprecipitates were probed for CLIP1, ZW10, CCAR1, USO1, and CCNB1. Experiments represent 2–4 replicates for each target.

M   Quantification of KIF11-CLIP1 co-immunoprecipitates from WT and RAB11-KD CaCo2 cells in three independent experiments.

N   Immunofluorescent staining for endogenous Clip1 (red) and Kif11 (green) in WT and Rab11 DKO mouse intestinal epithelial tissues. $n = 4$–5 mice for each genotype. White arrows point to Kif11$^+$ spindles. Scale bars, 20 μm.

O   Pearson's correlation of CLIP1 and KIF11 at mitotic spindles of WT and Rab11 DKO IECs. Results were analyzed from 21 and 13 mitotic cells in 5–10 independent microscopic images of WT and DKO tissues, respectively.

Data information: Two-way Anova was used in Fig 5D, one-way Anova was used in Fig 5G, and unpaired *t*-test was used in Fig 5H, M and O, where error bars represent SEM, and *$P < 0.05$; **$P < 0.01$; ***$P < 0.001$; ****$P < 0.0001$.

Source data are available online for this figure.

not been demonstrated previously, and we speculate that a similar mechanism may apply to other tissues. In DKO intestinal epithelia, we observed both an increased cell cycle entry and a mitotic arrest in the DKO tissues. Previous studies reported that Rab11a deficiency triggered a nuclear YAP translocation that could be the primary driver for a forced cell cycle entry (D'Agostino *et al*, 2019; Goswami *et al*, 2021). YAP activation regulates S-phase entry (Shen & Stanger, 2015) and YAP recruitment depends on a functional pre-Replicative Complex (preprint: García *et al*, 2021). These scenarios are consistent with the increased c-Myc, a direct YAP transcriptional target (Cai *et al*, 2018; Chen *et al*, 2018), and increased IdU labeling in DKO tissues. However, after the DKO cells entered cell cycle, they failed to properly form a bipolar spindle to complete the cell division. The failed mitotic division due to the spindle defect is consistent with the observed epithelial cell-autonomous death, loss of the rapid cycling stem cells, and lethality of the animals.

Endocytic trafficking reshapes the plasma membrane during cell division, which further partitions endocytic components along with the associated cargos (Furthauer & Gonzalez-Gaitan, 2009). The RAB11 recycling endosome system remained associated on vesicles throughout the cell cycle, with RAB11, pIgAR, and MYOSIN-Vb containing vesicles becoming clustered near the spindle poles after metaphase (Hobdy-Henderson *et al*, 2003). Disruption of RAB11 in mammalian cells, either by RNA interference or by a dominant negative plasmid, affected spindle pole protein localization, astral microtubules, and mitotic spindle orientation (Hehnly & Doxsey, 2014). The mouse work in this study validated these important concepts of mitotic regulation by Rab11 proteins by demonstrating their robust impact on tissue renewal and homeostasis. Our untargeted

Rab11a and Rab11b proteomic analysis revealed a large set of common proteins involved in cell cycle regulation, mitosis, and cytokinesis. Although we selected KIF11 in our phenotypic analysis, based on its high proteomic spectrum counts, our results suggest that loss of Rab11a and Rab11b likely perturbed a global distribution of mitotic recycling endosome and the assembly of spindle and pole protein networks. Our proteomic results suggested that Rab11a and Rab11b also coordinate the functions of other motor proteins such as MYH9 and MYH10, both of which regulate cytokinesis and cell motility (Wang *et al*, 2020).

Loss of Rab11a and Rab11b resulted in primarily monopolar spindles that mimicked the defects caused by KIF11 inhibitors. RAB11A and RAB11B mitotic endosomes may serve as a platform to coordinate the positioning, assembly, and functioning of multiple protein complexes at spindle poles and microtubules. Although KIF11 remains associated with spindle in Rab11-deficient cells, its function in driving the bipolar mitotic spindle (Acar *et al*, 2013) may be impaired. For instance, CLIP1 connects a subset of recycling endocytic vesicles to microtubules (Pierre *et al*, 1992), the endosome may further facilitate KIF11 and CLIP1 function at spindle poles where a complex may form at the growing plus end of spindle microtubule (Akhmanova *et al*, 2005). Likewise, the RAB11 endosome may provide a compartment to restrict or facilitate kinase reactions. The aurora-related protein kinase pEg2 of Xenopus laevis directly phosphorylates XlEg5 (a KIF11 homology) on a serine residue at its stalk domain (Giet *et al*, 1999). The phosphorylation at threonine 937 in KIF11 C-terminal tail by Cdk1-Cyclin B strongly increased its binding to microtubules *in vitro* (Cahu *et al*, 2008). Interestingly, we observed a strong association

between KIF11 and Cyclin B in Rab11-depleted cells, suggesting that Rab11 endosome regulates KIF11 interactions with other mitotic regulators.

Our study has limitations in resolving direct protein–protein interactions. The co-immunoprecipitation and untargeted proteomic approaches were not purposed for revealing direct binding
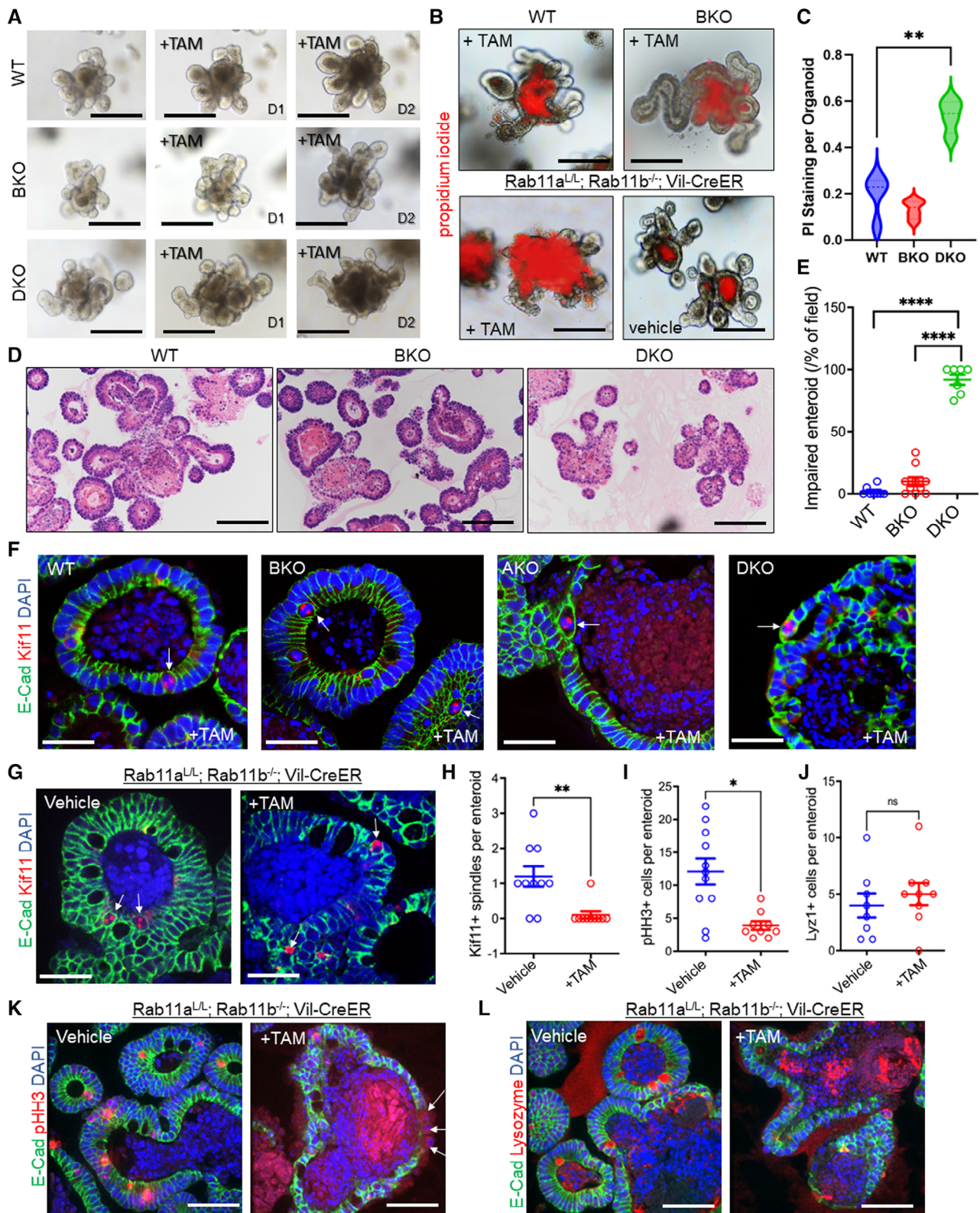

Figure 6.

Figure 6. Deletion of Rab11a and Rab11b from enteroids causes spindle defect and cell death.

A Enteroids were grown from mice of different genotypes. Images were taken before and after addition of 4-OHT that induces Rab11a deletion. Twenty–thirty images were taken daily from independent fields of cultures. Each genotype had replicates, and experiments were done twice. Scale bars, 500 μm.

B Propidium iodide (PI) staining of WT, BKO, and DKO enteroids 3 days after 4-OHT treatment *ex vivo*. Note DKO enteroids had increased PI staining along the epithelial edge. Vehicle-treated DKO enteroids were used as controls. Scale bars, 200 μm.

C PI-stained areas were normalized to total enteroid area for each enteroid of different genotypes.

D, E Histology sections of harvested enteroids of different genotypes were stained by H. & E. Enteroids showing impaired epithelial lining were scored from independent fields ($n = 8$, 10 and 7 for WT, BKO, and DKO, respectively) of biological replicates. Scale bars, 100 μm.

F, G Immunofluorescent staining for Kif11 (red) and E-cad (green) was performed on enteroids of various genotypes, all of which were treated with 4-OHT. Same experiments were done for DKO enteroids treated with vehicle or 4-OHT. White arrows point to Kif11$^+$ spindles. Scale bars, 20 μm.

H Normal bipolar Kif11 spindles were counted per enteroid of vehicle ($n = 10$) or 4-OHT treated DKO ($n = 10$) enteroids from biological replicates. Images were analyzed from two independent experiments.

I, J Numbers of pHH3$^+$ or Lyz1$^+$ cells were counted per enteroid of vehicle ($n = 11$ for pHH3; $n = 8$ for Lyz1) or 4-OHT treated DKO ($n = 9$ for both pHH3 and Lyz1) enteroids from biological replicates.

K, L Representative confocal fluorescent images of pHH3 (red) or Lyz1 (red) stained with E-Cad (green) from vehicle or 4-OHT treated DKO enteroids. Scale bars, 50 μm.

Data information: Unpaired *t*-test was used in Fig 6C, E, H, I and J, where error bars represent SEM, and *$P < 0.05$; **$P < 0.01$; ****$P < 0.0001$.

Source data are available online for this figure.

targets. The intracellular association between KIF11 and RAB11 is likely mediated by intermediate partners, such as tubulin, dynactin, or FIPs, which interact with both proteins (Zhang *et al*, 2008b; Ai *et al*, 2009; Hehnly & Doxsey, 2014). The KIF11 stalk contains coiled-coil motif and, when overexpressed in cells, was able to co-immunoprecipitate with both Rab11a and Rab11b. Almost all Rab11 FIPs use their conserved C-terminal coiled-coil domain to bind Rab11 (Hales *et al*, 2001). Resolved complex structures of Rab11–FIP2, Rab11–FIP3, Rab14–FIP1, and Rab25–FIP2 suggested that all of the Rab11 binding domains contain a central parallel coiled coil (Wei *et al*, 2006; Lall *et al*, 2015; Kearney & Khan, 2020). FIP3 localizes to mitotic spindle (Hehnly & Doxsey, 2014), forms homo-oligomers, and its recruitment to recycling endosome by Rab11 is essential for cytokinesis (Eathiraj *et al*, 2006). FIP3's Rab11 binding domain contains a coiled-coil homodimer with two symmetric interfaces binding to two Rab11 molecules (Shiba *et al*, 2006). The C- and N-terminal domains of the homodimeric CLIP1 are also connected by a long coiled coil

(Pierre *et al*, 1992). Interestingly, aurora-related protein kinase directly phosphorylates a residue at KIF11's stalk region (Giet *et al*, 1999). A direct association between KIF11 and dynactin [p150(Glued)] was previously isolated in yeast two-hybrid study using the stalk-tail region (420–811 aa.) as a bait (Blangy *et al*, 1997). Coincidentally, dynactin directs Rab11 recycling endosomes to pericentrosomal region and spindle (Ai *et al*, 2009). Furthermore, DENN/MADD (Rab3-GEP) directly binds to the stalk domain of microtubule motors, KIF1Bbeta and KIF1A, to transport synaptic vesicles (Niwa *et al*, 2008). These studies suggest that the coiled-coil motif of KIF11 stalk region may interface with various Rab11-interacting partners in a spindle microtubule-associated complex.

USO1(p115) interacts with γ-tubulin to regulate centrosomal targeting during mitosis (Radulescu *et al*, 2011). Disruption of USO1 leads to spindle collapse, chromosome mis-segregation, and failed cytokinesis (Radulescu *et al*, 2011). It is plausible that pole organizers such as USO1, with the help of RAB11 endosome, could

Figure 7. Loss of Rab11a and Rab11b activates apoptosis program.

A Immunohistochemistry for cleaved caspase 3 (CC3) was performed on TAM-treated enteroids of different genotypes. Black arrows point to CC3$^+$ cells at the epithelial lining of DKO enteroids. Scale bars, 50 μm.

B Quantification of number of CC3$^+$ cells within epithelial lining of enteroids of different genotypes and treatments. $N = 9$ for WT, BKO, BKO + TAM, and DKO; $n = 7$ for WT + TAM; $n = 11$ for DKO + TAM of biological replicates.

C Heat map of apoptotic genes in WT and Rab11 DKO intestinal transcriptomes ($n = 3$ for each genotype).

D GSEA analysis shows significantly enriched apoptotic gene set in Rab11 DKO intestinal epithelia compared with WT littermates. $P < 0.001$.

E–H Representative apoptotic genes, Anxa1, Anxa5, Bcl2l1, Bcl10, which were highly elevated in DKO intestines. $n = 3$ mice for each genotype.

I Immunofluorescent staining for CC3 (green) was performed on WT and Rab11 DKO intestinal epithelial tissues before and after tamoxifen treatment. Scale bars, 50 μm.

J Quantification of CC3-positive cells per crypt-villus axis in WT and Rab11 DKO intestines. Results were obtained from 10 to 15 independent microscopic images taken from 4 to 5 mice for each genotype.

K Heat map of TNFA-NFκB pathway genes in WT and Rab11 DKO intestinal transcriptomes ($n = 3$ for each genotype).

L Tnf transcripts were highly elevated in DKO intestines. $n = 3$ mice for each genotype.

M GSEA analysis shows significantly enriched TNFA-NFκB pathway gene set in Rab11 DKO compared with WT littermates.

N Immunohistochemistry for NFκB was performed on WT and Rab11 DKO intestinal tissues.

O Quantification of ratio of nuclear NFκB$^+$ cell number over total IECs per crypt-villus axis. Data were analyzed from 10 to 15 independent microscopic fields. $n = 4$–5 mice for each genotype.

P Immunofluorescent staining for p53 (green) and E-cad (red) in WT and Rab11 DKO intestinal tissues. Scale bars, 50 μm, 20 μm.

Data information: Unpaired *t*-test was used in Fig 7J and O. One-way Anova was used in Fig 7B, E–H and L, where error bars represent SEM, and **$P < 0.01$; ***$P < 0.001$; ****$P < 0.0001$.

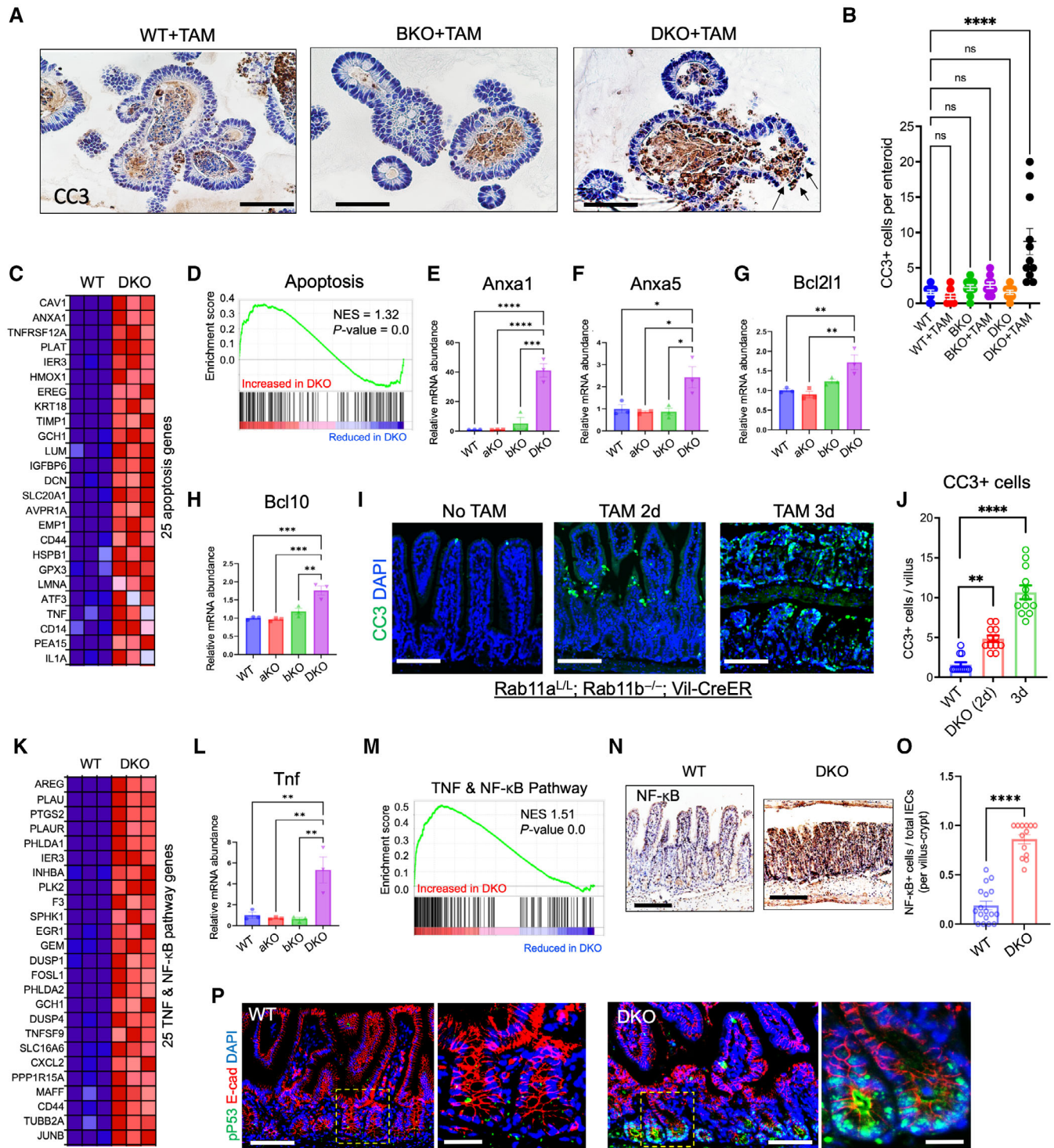Source data are available online for this figure.

Figure 7.

locate KIF11 to the centrosome allowing it to drive apart the spindle poles. Without RAB11, kinetochore microtubules may never form because of the lack of a bipolar spindle. A robust KIF11 and Cyclin B interaction in RAB11-depleted cells was reminiscent of nocodazole treatment that activates spindle checkpoint and elevates Cyclin B for 48 h (Choi *et al*, 2011). Future studies will determine if and how Rab11a and Rab11b may regulate the development and maintenance of other tissues.

Materials and Methods

Mice

Rab11a^flox (Yu *et al*, 2014b), *Villin-CreER* (el Marjou *et al*, 2004), and *Villin-Cre* mice (Madison *et al*, 2002) have been previously described. Littermate mice were used for comparison in all experiments. For each experiment, at least three mice per group were used, and experiments were repeated for 3–5 times using different litters on independent occasions. Animal experiments were conducted in accordance with NIH guidelines and approved by the Institutional Animal Care and Use Committee (IACUC) at Rutgers University.

Derivation of Rab11b knockout mice by CRISPR-CAS editing

Female mice (C57BL/6J, 4–5 weeks old) were used as embryo donors for superovulation. After mating, fertilized embryos were collected and microinjected directly into the pronucleus with a mix of two sgRNAs and Cas9 mRNA (Sigma-Aldrich). The first gRNA target sequence is 93 bp upstream of Rab11b exon2 TCCGTGGGT GGCAGAAATC. The second gRNA target sequence is 88 bp downstream of Rab11b exon4 CCGGGTCTGGGTGGCCGTT. 25 ng/μl of each sgRNA and 50 ng/μl of Cas9 mRNA were mixed in RNase-free injection buffer (Specialty Media) and microinjected directly into the pronucleus of zygotes in M2 medium as previously described (Wang *et al*, 2013a,b; Yang *et al*, 2014). The injected embryos were cultured in KSOM-AA medium at 37°C with 5% CO_2. 20–25 microinjected embryos were transferred into oviducts of pseudo-pregnant CD-1 females (Charles River). 1–2 mm of tails biopsies from 10-day-old live pups were collected for extraction of genomic DNA using HotShot method as previously described (Truett *et al*, 2000). For genotyping, mouse genomic DNA was used as template with Advantage2 polymerase mix (Takara) for PCR reactions. Target regions (~500 bp) were amplified by PCR primers either flanking exon 2 and exon 4 or primers overlapping large deletion between the two exons. Most sites were amplified successfully after 33 cycles at 94°C for 20 s and one step annealing/extension at 68°C for 1 min. PCR products were analyzed by agarose gel electrophoresis to verify amplicon size. To determine genome targeting efficiency, indel (insertion/deletion) mutations generated by CRISPR/Cas9 were detected first with T7 endonuclease I (New England biolabs) assays and then through direct sequencing of the PCR products. Briefly, 5 μl of PCR reaction was denatured and reannealed according to manufacturer protocol, 95°C 5 min, ramp 95°C to 85°C at 2°C/s, then ramp from 85 to 25°C at 0.1°C/s, hold at 4°C. T7 endonuclease I digestion was conducted in 20 μl reaction at 37°C for 20 min using NEB buffer2 plus 5 units of T7 enzyme in addition to the 5 μl of reannealed PCR products. The digestion reactions were electrophoresed using a 2% agarose gel. All PCR amplicons from mouse founders with positive T7 endonuclease I digestion were cloned for sequencing. Target region amplicons were cloned into a TA-cloning vector (Invitrogen) and transformed into *E. coli* competent cells (New England Biolabs). Plasmid DNA was isolated and sequenced by commercial sequencing company. Founder mice with large deletion overlapping exon 2 and exon 4 or exon 2 deletion were backcrossed to C57BL/6J for three generations before interbreeding litter mates to produce homozygous *Rab11b^−/−* alleles. For genotyping

Rab11b mouse colonies, mouse genomic DNA was used as template with GoTaq Flexi Polymerase kit (Promega M8298) for PCR reactions. A triple primer PCR mixture was used to detect wild-type allele target region (505 bp) using primers R11BE2F: CATTCTTGA CTTACTCAGCTGTCA & R11BE2R: TGCTATCTCTAGGTCTTGACCC TA flanking exon 2 or Rab11b deletion target region (410 bp) by primers R11BE2F: CATTCTTGACTTACTCAGCTGTCA & R11BE4R: GAGGTTCCCAGGCACAGCCAAGT flanking exon 2 and exon 4. Sites were amplified using a thermocycler with denaturing at 94°C for 30 s, annealing at 56°C for 30 s and extension at 72°C for 1 min repeated for 35 cycles. PCR products were analyzed by 1.5% agarose gel electrophoresis to verify amplicon size.

Cell culture, transient transfection, and chemical treatment

HEK293T cells were grown in Dulbecco's Modified Eagle's Medium (DMEM) (Corning, CM10013) supplemented with 10% fetal bovine serum (FBS) (GIBCO, A3160501). Cells were transiently transfected with plasmids using Lipofectamine 3000 (Invitrogen, L3000008). For KIF11 inhibitor treatment, cells were treated with 50 μM Monastrol, 2.5 μM STLC or 100 nM Ispinesib dissolved in DMSO, or by DMSO alone as a control. After 24 h, cells were fixed for immunostaining and imaging or for co-IP analysis. The control and RAB11-knockdown Caco-2 cells have been described previously (D'Agostino *et al*, 2019).

RNA extraction, bulk RNA sequencing, and gene set enrichment analysis

At 3 months of age, Rab11a^Fl/Fl^ (control), Rab11a^Fl/Fl^; Villin-CreER (aKO), Rab11b^−/−^ (bKO), and Rab11a^Fl/Fl^; Rab11b^−/−^; Villin-CreER (DKO) mice were intraperitoneally injected with 1 mg tamoxifen dissolved in corn oil ($n = 3$ for each genotype). Two days after tamoxifen injection, mouse small intestines were dissected and snap-frozen in liquid nitrogen. The tissue was stored at −80°C until RNA isolation. For total RNA extraction, 2–3 mm of jejunum was immersed in 800 μl RLT Buffer (included with Qiagen RNeasy Plus Mini Kit #74134) with 10 μM β-Mercaptoethanol. Tissue homogenization was performed by passing tissues through a 20-gauge needle (BD 305176) on the ice. The remaining isolation procedure was completed according to the Qiagen RNeasy Mini protocol. RNA was eluted from the spin column using 30 μl of RNase-free water and passed quality control before sequencing.

For GSEA analysis (Subramanian *et al*, 2005), molecular signature database (MSigDB) was used to generate heat maps and leading-edge enrichment plots. One thousand permutations were performed on each gene list tested and normalized enrichment score (NES), and nominal *P*-value was reported for each analysis.

Enteroid culture procedure

Enteroid culture followed the procedures reported previously (Sato & Clevers, 2013). Adult mice of 3–6 months of age were euthanized. Small intestines were opened longitudinally, and jejuna were cut into 2–3 mm pieces. Tissues were then gently shaken in ice-cold 10 mM EDTA in HBSS at 4°C for 30 min followed by a vigorous shaking to release epithelia. The supernatant was then passed through a sterile 70 μm cell strainer

(Corning; 352350). To remove single cells from the filtrate, the pellet was subjected to three rounds of washing in 10 ml of basal culture medium (2 mM GlutaMax 10 mM HEPES 100u/ml PenStrep in DMEM/F12) and centrifuged at 200 g for 2 min at 4°C. The total number of crypts was counted and plated at a concentration of 200 crypts in every 30 μl of Matrigel on an 8-well glass bottom chamber. The crypts were grown in IntestiCult Organoid Growth medium (Stem Cell Technologies; 06005) with the culture medium changed every 24 h. On Day 3 of organoid culture, the IntestiCult medium was supplemented with 0.5 μM (Z)-4-hydroxytamoxifen (4-OHT, Sigma; H7904) to induce *Rab11a* deletion. After overnight incubation with 4-OHT, culture was changed to a normal IntestiCult medium and grown until Day 7.

For propidium iodide staining, live organoid cultures were treated at a final concentration of 50 μg/ml propidium iodide for 30 min on Day 7 and then washed with PBS 3 times before imaging with a Nikon Eclipse TE2000-U bright-field inverted microscope.

For embedding the organoids, the Matrigel was dissolved and removed by Corning Recovery Solution (Corning; 354253). Organoids were further centrifuged at 200 g for 5 min and washed with cold PBS, 2-min centrifugation at 200 g. Crypts were then resuspended in 4% paraformaldehyde and centrifuged at 200 g for 5 min followed by a cold PBS wash and resuspension in Matrigel forming clump of organoids and left at 37°C to solidify. Once solid, 70% ethanol was added and stored at 4°C until paraffin embedding at the Histology Core of Rutgers Behavioral and Health Science, New Jersey Medical School.

Lysate preparation and western blot analysis

Cells were washed twice with PBS, lysed in lysis buffer (50 mM Tris–HCl, pH7.4, 150 mM NaCl, 1 mM EDTA, 1× Roche proteinase inhibitor cocktail, and 0.1% NP-40), and scraped by a rubber spatula. Cell lysates were sonicated with Qsonica XL-2000 sonicator at intensity setting of 3 for 10 s. Protein concentrations were determined by Bradford assay. Protein samples were heat-denatured in LDS with 10% β-mercaptoethanol. Equal amounts of protein samples were resolved by SDS–PAGE.

Intestinal tissues were placed in 500 μl lysis buffer (50 mM Tris–HCl, pH 7.5, 150 mM NaCl, 10 mM EDTA, 0.02% NaN3, 50 mM NaF, 1 mM NaN$_3$VO$_4$, 0.5% PMSF, 0.5 mM DTT) and 1 tablet of inhibitor for protease (11836170001, Sigma) and phosphatase (04906845001, Sigma). Samples were sonicated using a Qsonica XL-2000 sonicator. Homogenized tissue lysates were centrifuged at 13,000 rpm for 10 min at 4°C, and the supernatant was collected.

For western blot analysis, tissue or cell lysates were resolved in SDS–PAGE gels, transferred to 0.4 μm nitrocellulose membranes at 4°C. Membranes were blocked for 1 h in Tris-buffered saline (TBS) 0.1% Tween-20 (TBST) containing 5% nonfat dry milk, at room temperature. The membrane was then incubated overnight at 4°C in primary antibody diluted in blocking buffer. The membrane was washed with TBST and incubated with HRP-conjugated secondary antibody diluted in blocking buffer for 1 h at room temperature. Membranes were rinsed in TBST before incubation with ECL solution in dark and developed using the Bio-Rad Chemi-Doc Imaging System (version 2.4.0.03). For western blot antibody concentrations, see Appendix Table S1.

Co-immunoprecipitation (co-IP) and proteomic analysis

Oligonucleotide sequences for three copies of FLAG sequence (DYKDDDDK) were inserted into Not I/Age I sites of the pQCXIP vector (Clontech), referred to as pQCXIP-3 × FLAG vectors. Coding sequences for *Rab11a* and *Rab11b* were then inserted into Age1/Not1 sites in the pQCXIP-3 × FLAG vectors. The resulting 3 × FLAG-Rab11a-pQCXIP and 3 × FLAG-Rab11b-pQCXIP vectors were sequence-verified. 3 × FLAG-pQCXIP, 3 × FLAG-Rab11a-pQCXIP, and 3 × FLAG-Rab11b-pQCXIP were transfected into HEK293T cells. Twenty-four-hour post-transfection, cells were washed twice with PBS and lysed in 50 mM Tris–HCl, pH7.4, 150 mM NaCl, 1 mM EDTA, 1 × Roche proteinase inhibitor cocktail, and 0.1% NP-40. Protein concentrations were determined by Bradford assay, and 2 mg of total lysate protein was used for an overnight immunoprecipitation reaction with 40 μl of prewashed anti-Flag M2 affinity gel beads (A2220, Sigma) at 4°C. The beads and associated complexes were pelleted by centrifugation at 8,200 g for 1 min and washed three times by 50 mM Tris–HCl pH 7.4 and 150 mM NaCl. Protein samples were denatured in LDS and resolved by SDS–PAGE. For proteomic analysis, Ruby Red staining was performed and protein bands at 25 kDa and higher were subjected to in-gel digestion and mass spectrometry. Heat maps of proteomic results based on spectrum counts and unique peptide numbers were generated by the "pheatmap" R package.

For IP of endogenous KIF11 from control and RAB11KD Caco2 cells, lysates were first precleared by the addition of a 50 μl bead slurry (Santa Cruz) to 2 mg of lysate, and incubation for 30 min at 4°C with gentle agitation. The mixture was centrifuged at 14,000 g for 10 min. The precleared supernatant was added to 50 μl of bead slurry that was already conjugated with 5 μg of KIF11 antibody. We also performed negative control IP reactions, where no KIF11 antibody was added in the pull-down assay. The precipitation mixture was suspended and incubated for overnight at 4°C. The mixtures were then washed three times with 50 mM Tris–HCL (pH 7.4) and 150 mM NaCl and centrifuged. Bound proteins were eluted in LDS loading buffer (NP0008, NuPAGE) and resolved by SDS–PAGE. For proteomic analysis, eluted proteins were subjected to mass spectrophotometry as described above. We have used negative control proteomic results for subtracting nonspecific background from the KIF11 proteomics.

Cloning of V5-tagged KIF11 truncates

To construct V5-tagged KIF11 truncated proteins, cDNA sequences for KIF11 fragments corresponding to the motor (1–1,162 bp), stalk (1,162–2,584 bp), and tail (2,320–3,168 bp) domains were amplified from the mEmerald-Kinesin11-N18 plasmid (Addgene 54137). The primers used for individual fragments were as follows:

Motor-Forward 5′-CACCATGGCGTCGCAGCCAAATTCG;
Motor-Reverse 5′-CCCTCGTTTTAAACGTTCTATCTCCTCCG;
Stalk-Forward 5′-CACCATGGATCTTGCTGCAGCCCGT;
Stalk-Reverse 5′-GTCTGAACTTGAAGCCTCACACC;
Tail-Forward 5′-CACCATGGCTGATTCTGATGGCTTCTCAC;
Tail-Reverse 5′-AAGGTTGATCTGGGCTCGCA.

The amplified region is then inserted into the pcDNA3.1D/V5-His-TOPO (Thermo Fisher K49001). The resulting plasmids were sequence-verified.

In vitro binding assays

For *in vitro* binding of V5-tagged KIF11 fragments to Rab11a and Rab11b recombinant proteins, KIF11 fragments were transcribed and translated *in vitro* using the TnT Quick Coupled Transcription/Translation Kit (Promega, L1170). Reaction comprised 40 µl of TnT Quick Master Mix, +1 µl of Methionine, 1 mM, and 2 µg of plasmids encoding motor, stalk, and tail domains. TnT reactions were performed for 90 min at 30°C. For binding, individual TnT reactions were added to 300 ng of Rab11a (Origene, TP300352) or Rab11b (Origene, TP322162) recombinant proteins immobilized on agarose beads via anti-Myc antibody. Binding was performed at 4°C overnight. Beads were washed in binding buffer for four times and denatured in LDS, and elutes were loaded on SDS–PAGE. Blots were probed for V5 and then reprobed for RAB11.

For KIF11-RAB11 *in vitro* binding assays, 300 ng of full-length recombinant KIF11 (Origene, TP318842) was immobilized on Protein G-agarose beads (Sigma, Ref 11719416001) via a KIF11 antibody (Sigma HPA010568). Three hundred nanogram of recombinant Rab11a (Origene, TP300352) and Rab11b (Origene, TP322162) was then added to binding buffer (50 mM Tris–HCl, pH 7.4, 150 mM NaCl and 1 mM EDTA, 1% Triton X-100) in the presence or absence of 0.2 mM of GTPγS (Cytoskeleton, Inc #BS01) and 1 mM GDP (EMD Millipore, 20–177). Twenty microliter of dry bead volume was used for each reaction, which also contained 1 µg BSA to suppress nonspecific binding. Binding was performed at 4°C overnight. Beads were washed in binding buffer for four times and denatured in LDS, and elutes were loaded on SDS–PAGE. Blots were probed with anti-RAB11 and reprobed with anti-KIF11 antibodies.

Histology and immunofluorescent analysis

Formalin-fixed paraffin-embedded intestinal tissue sections were heated at 55°C for 15 min, deparaffinized in Xylene, rehydrated in an ethanol gradient to 50%, and rinsed in deionized water. For hematoxylin and eosin staining, slides were incubated in hematoxylin for 3–5 min and washed in running deionized water for 5 min. Slides were then incubated in eosin for 2 min and dehydrated in increasing concentrations of ethanol: 50%, 70%, 75%, 95% (2 times), 100% (2 times), and Xylene (2 times) for 20 dips each. Dehydrated tissue slides were mounted using Cytoseal 60 (Thermo Scientific 8310-4) and cover-slipped. For Alcian blue staining, rehydrated tissue slides were incubated in 3% Alcian blue 8GX (Sigma, A5268, pH 2.5) for 30 min and then washed in running deionized water for 5 min. Tissue slides were counterstained with Nuclear red (Vector laboratories H-3403-500) for 5 min, dried, and mounted as described above.

For immunofluorescent staining, formalin-fixed paraffin-embedded tissue sections were deparaffinized and rehydrated as described above. Antigen retrieval was carried out in monohydrate citric acid buffer (pH 6) by boiling slides for 15 min. Once cooled to 40°C, slides were washed in deionized water for 5 min followed by PBS wash for 5 min. Slides were incubated for 1 h with blocking solution (0.1% Triton-X100, 2% BSA, 2% normal donkey or goat serum in PBS) followed by

incubation in primary antibody diluted in blocking solution overnight at 4°C. Antibodies and concentrations are listed in the appendix. Slides were washed three times, 10 min each, in PBS and then incubated in secondary antibodies diluted in blocking solution at room temperature for 1 h. After incubation, slides are washed two times, 10 min each, in PBS. Slides were counterstained with DAPI for 15 min, rinsed in PBS, and mounted using Prolong Gold Antifade (Invitrogen P36930). When staining for alkaline phosphatase, slides were incubated in 125 mM Tris–HCl (pH 8.4) containing 0.5% Vector red substrate (2 drops of reagent 1, 2 drops of reagent 2, and 2 drops of reagent 3) for 30 min after rehydration. Slides were then washed in running deionized water for 5 min and were continued to antigen retrieval and subsequent staining steps as described above. When staining for phosho-p53, an additional tyramide signal amplification (TSA) step was introduced after rehydration and washing. Before wash, the slides were first quenched for endogenous peroxidase activity in methanol containing 3% H_2O_2 at room temperature. Antigen retrieval step was then performed by placing slides in DAKO target retrieval solution (Agilent S1699). Slides were then boiled in a rice cooker for 15 min. For TSA, secondary antibodies used were HRP-conjugated, and following incubation for 1 h, slides were washed in PBS for 10 min three times. Slides were then incubated in TSA working solution containing 1% H_2O_2 and AF488 conjugated TSA at a concentration of 1:200 in 1× amplification buffer (provided with kit) for 15 min. Slides were then washed with PBS for 10 min three times, and other desired antibodies, such as E-cadherin, were added for overnight incubation. Following the second primary incubation, slides were washed and incubated with secondaries and mounted as described above.

For indirect immunofluorescent staining of HEK293T cells, cells were fixed in 4% paraformaldehyde, permeabilized with 0.3% Triton X-100 in PBS, and blocked in PBS with 5% normal donkey serum. Cells were then incubated with specific primary antibodies diluted in blocking buffer with 2% BSA at 4°C overnight. Slides were washed with PBS and incubated with secondary antibodies diluted in blocking buffer for 1 h at room temperature, washed in PBS, dried, and mounted using Prolong Gold, and covered. Images were taken on Zeiss LSM 510 and 980. Images were analyzed using ImageJ (NIH). For antibody concentrations, please see Appendix Table S1.

Immunohistochemistry

Formalin-fixed paraffin-embedded intestinal tissue sections were rehydrated as described above. Tissue slides were quenched for endogenous peroxidase activity in a 3% hydrogen peroxide in methanol solution for 5 min. Antigen retrieval was performed in boiling monohydrate citric acid buffer (pH 6) for 15 min using a microwave and cooled to 40°C. Slides were washed under running water for 5 min, washed in PBS for 5 min, and then blocked for nonspecific antibody binding in PBS with 2% BSA, 10% Triton-X100 and 2% donkey serum for 1 h. Primary antibody in blocking solution was added and incubated at 4°C overnight; concentrations are listed in the appendix. After overnight incubation, tissue slides were washed in PBS for three times, 10 min each. Biotin conjugated secondary antibody was added in blocking solution, incubated for 1 h at room temperature, and washed three times for 10 min each wash. Slides were then incubated in an avidin–biotin complex (ABC) solution containing two drops of reagent A and two drops of reagent B

(Vector Labs ABC standard kit, SK-4100) in 5 ml of PBS (ABC solution was prepared 30 min prior to use) for 1 h. Tissue slides were then washed in PBS for 10 min for three times, and incubated in DAB solution containing two drops of buffer, pH 7.4, four drops of DAB substrate, and two drops of hydrogen peroxide. DAB reaction time was antigen-specific, ranging in time from 30 s to 5 min. Following DAB incubation, slides were placed in deionized water and washed for 5 min. Tissue slides were incubated in Hematoxylin QS (Vector Labs, H3404) for 3 min and washed in deionized water for 5 min. Tissue slides were dehydrated in the reverse concentration of ethanol. Following Xylene slides were mounted with Cytoseal 60 (Thermo Scientific 8310-4) and cover-slipped.

Propidium iodide (PI) cell cycle analysis

The intestinal epithelial cells were isolated as described above in enteroid culture section. Adult mice of 3–6 months of age were sacrificed. Intestinal epithelial tissues were released in 10 mM EDTA in HBSS. The supernatant was passed through a wire mesh to remove residual tissue pieces from release epithelium. The supernatant was then pelleted, washed in cold HBSS, and pelleted again before being treated with 10 ml of TrypLE with DNase. The mixture was left to digest in a 37°C water bath for 20 min and shaken every 5 min. After digestion, cells were washed and fixed on ice in 70% ethanol for 2 h. The fixed cells were then briefly washed in PBS before incubating cells at room temperature with 1 ml of PI staining solution (0.1% Triton X-100, 50 μg/ml Propidium Iodide, and 100 μl of RNase cocktail) for 30 min. Following incubation, cells were washed and resuspended in 500 μl of FACS buffer. Cells were characterized for propidium iodide content with flow cytometer, and the data were analyzed using the cell cycle analysis function on FlowJo v10.

In vivo CldU and IdU labeling experiments

Adult mice were injected with tamoxifen intraperitoneally. Twenty-four hours later, mice were injected with CldU (5-Chloro-2′-deoxyuridine) intraperitoneally at 24 h. After 1–1.5 days, WT and DKO mice were sacrificed in pairs 3 h after an injection of IdU (5-Iodo-2′-deoxyuridine) to label new dividing cells.

Live cell imaging

Live cells were transfected with mCherry-tagged Rab11a constructs. 12–16 h after transfection, cells were labeled by SiR-Tubulin (Cytoskeleton, CY-SC002) for tubulin at a final concentration of 100 nM. Two hours later, cells were used for imaging on a Zeiss Cell Observer SD, 63 × Plan-Apo 63× 1.4 NA objective; and Photometrics Evolve camera. Z-stack images were acquired using a 2 μm steps. Live cell culture conditions were set to 37°C with 5% CO_2 and maintained during image acquisition.

Image analysis and scoring of mitotic spindle morphology

Immunohistochemistry (IHC) images were processed using the IHC tool in ImageJ. Images were converted to 8-bit grayscale. Regions of interest (ROI) were hand-drawn, and grayscale values for each pixel in ROI determined. The grayscale distribution of pixels within images was derived from these values, and the percent of pixels within ROIs of each image at a greyscale intensity of 165 or higher was calculated. For quantification of the mean gray intensity of fluorescent images, signals were first converted to grayscale. Mean gray intensity was measured in ROIs. For quantification of Alcian blue-, cleaved Caspase-, pHH3-, CldU-, and IdU-positive cells. the numbers of positive cells were counted for each crypt-villus axis. For scoring of mitotic spindle morphology in tissue sections or cell culture, the number of bipolar, monopolar, tripolar spindles was counted for each group. Percentage of a specific morphology was calculated based on total spindle numbers and depicted as stacking bar graphs.

Quantification and statistical analysis

For mouse study, each experiment contained 3–6 mice per group. Experiments were typically repeated 2–4 times. Quantification of immunostaining results was reported from 10 to 12 independent microscopic fields of at least three mice for each condition. Densitometry quantification of western blots was performed by ImageJ from independent experiments. Pearson's Correlation was performed by launching ImageJ and opening images to be analyzed. Images were split into multiple channels using the image/split channel function. A region of interest (ROI), in this case the spindle poles defined by pericentrin, was drawn. Analyze/Coloc 2 functions were then used on channels of interest. The Costes' randomization was then set to 50, and Pearson's R-value (no Threshold) was recorded. All statistical analysis was done using the GraphPad Prism software unpaired t-tests for 2-group comparison, and one-way ANOVA test for multigroup analysis.

Data availability

The RNA-Seq datasets are available in Gene Expression Omnibus, accession number: GSE232493 (https://www.ncbi.nlm.nih.gov/geo/query/acc.cgi?acc=GSE232493). The mass spectrometry proteomics data have been deposited to the ProteomeXchange Consortium via the PRIDE partner repository with the dataset identifier PXD042300 and PXD042335.

Expanded View for this article is available online.

Author contributions

Ivor G Joseph: Conceptualization; data curation; formal analysis; validation; investigation; visualization; methodology; writing – original draft; writing –

Disclosure and competing interest statement

References

Acar S, Carlson DB, Budamagunta MS, Yarov-Yarovoy V, Correia JJ, Niñonuevo MR, Jia W, Tao L, Leary JA, Voss JC *et al* (2013) The bipolar assembly domain of the mitotic motor kinesin-5. *Nat Commun* 4: 1343

Ai E, Poole DS, Skop AR (2009) RACK-1 directs dynactin-dependent RAB-11 endosomal recycling during mitosis in Caenorhabditis elegans. *Mol Biol Cell* 20: 1629–1638

Akhmanova A, Mausset-Bonnefont AL, van Cappellen W, Keijzer N, Hoogenraad CC, Stepanova T, Drabek K, van der Wees J, Mommaas M, Onderwater J *et al* (2005) The microtubule plus-end-tracking protein CLIP-170 associates with the spermatid manchette and is essential for spermatogenesis. *Genes Dev* 19: 2501–2515

Arnal I, Heichette C, Diamantopoulos GS, Chrétien D (2004) CLIP-170/tubulin-curved oligomers coassemble at microtubule ends and promote rescues. *Curr Biol* 14: 2086–2095

Baetz NW, Goldenring JR (2013) Rab11-family interacting proteins define spatially and temporally distinct regions within the dynamic Rab11a-dependent recycling system. *Mol Biol Cell* 24: 643–658

Bannigan A, Scheible WR, Lukowitz W, Fagerstrom C, Wadsworth P, Somerville C, Baskin TI (2007) A conserved role for kinesin-5 in plant mitosis. *J Cell Sci* 120: 2819–2827

Bettess MD, Dubois N, Murphy MJ, Dubey C, Roger C, Robine S, Trumpp A (2005) c-Myc is required for the formation of intestinal crypts but dispensable for homeostasis of the adult intestinal epithelium. *Mol Cell Biol* 25: 7868–7878

Bhartur SG, Calhoun BC, Woodrum J, Kurkjian J, Iyer S, Lai F, Goldenring JR (2000) Genomic structure of murine Rab11 family members. *Biochem Biophys Res Commun* 269: 611–617

Blangy A, Arnaud L, Nigg EA (1997) Phosphorylation by p34cdc2 protein kinase regulates binding of the kinesin-related motor HsEg5 to the dynactin subunit p150. *J Biol Chem* 272: 19418–19424

Bravo-Cordero JJ, Marrero-Diaz R, Megías D, Genís L, García-Grande A, García MA, Arroyo AG, Montoya MC (2007) MT1-MMP proinvasive activity is regulated by a novel Rab8-dependent exocytic pathway. *EMBO J* 26: 1499–1510

Busch KE, Hayles J, Nurse P, Brunner D (2004) Tea2p kinesin is involved in spatial microtubule organization by transporting tip1p on microtubules. *Dev Cell* 6: 831–843

Cahu J, Olichon A, Hentrich C, Schek H, Drinjakovic J, Zhang C, Doherty-Kirby A, Lajoie G, Surrey T (2008) Phosphorylation by Cdk1 increases the binding of Eg5 to microtubules *in vitro* and in Xenopus egg extract spindles. *PLoS One* 3: e3936

Cai J, Song X, Wang W, Watnick T, Pei Y, Qian F, Pan D (2018) A RhoA-YAP-c-Myc signaling axis promotes the development of polycystic kidney disease. *Genes Dev* 32: 781–793

Casanova JE, Wang X, Kumar R, Bhartur SG, Navarre J, Woodrum JE, Altschuler Y, Ray GS, Goldenring JR (1999) Association of Rab25 and Rab11a with the apical recycling system of polarized Madin-Darby canine kidney cells. *Mol Biol Cell* 10: 47–61

Chen X, Gu W, Wang Q, Fu X, Wang Y, Xu X, Wen Y (2018) C-MYC and BCL-2 mediate YAP-regulated tumorigenesis in OSCC. *Oncotarget* 9: 668–679

Choi HJ, Fukui M, Zhu BT (2011) Role of cyclin B1/Cdc2 up-regulation in the development of mitotic prometaphase arrest in human breast cancer cells treated with nocodazole. *PLoS One* 6: e24312

D'Agostino L, Nie Y, Goswami S, Tong K, Yu S, Bandyopadhyay S, Flores J, Zhang X, Balasubramanian I, Joseph I *et al* (2019) Recycling endosomes in mature epithelia restrain tumorigenic signaling. *Cancer Res* 79: 4099–4112

Desclozeaux M, Venturato J, Wylie FG, Kay JG, Joseph SR, Le HT, Stow JL (2008) Active Rab11 and functional recycling endosome are required for E-cadherin trafficking and lumen formation during epithelial morphogenesis. *Am J Physiol Cell Physiol* 295: C545–C556

Eathiraj S, Mishra A, Prekeris R, Lambright DG (2006) Structural basis for Rab11-mediated recruitment of FIP3 to recycling endosomes. *J Mol Biol* 364: 121–135

Fan GH, Lapierre LA, Goldenring JR, Sai J, Richmond A (2004) Rab11-family interacting protein 2 and myosin Vb are required for CXCR2 recycling and receptor-mediated chemotaxis. *Mol Biol Cell* 15: 2456–2469

Fawley J, Gourlay DM (2016) Intestinal alkaline phosphatase: a summary of its role in clinical disease. *J Surg Res* 202: 225–234

Feng Q, Bonder EM, Engevik AC, Zhang L, Tyska MJ, Goldenring JR, Gao N (2017) Disruption of Rab8a and Rab11a causes formation of basolateral microvilli in neonatal enteropathy. *J Cell Sci* 130: 2491–2505

Ferro E, Bosia C, Campa CC (2021) RAB11-mediated trafficking and human cancers: an updated review. *Biology (Basel)* 10: 26

Folker ES, Baker BM, Goodson HV (2005) Interactions between CLIP-170, tubulin, and microtubules: implications for the mechanism of Clip-170 plus-end tracking behavior. *Mol Biol Cell* 16: 5373–5384

Furthauer M, Gonzalez-Gaitan M (2009) Endocytosis and mitosis: a two-way relationship. *Cell Cycle* 8: 3311–3318

García RM, Haccard O, Chesneau A, Narassimprakash H, Roger JE, Perron M, Marheineke K, Bronchain O (2021) A non-transcriptional function of Yap orchestrates the DNA replication program. *bioRxiv* https://doi.org/10.1101/2021.11.18.468628 [PREPRINT]

Giet R, Uzbekov R, Cubizolles F, Le Guellec K, Prigent C (1999) The *Xenopus laevis* aurora-related protein kinase pEg2 associates with and phosphorylates the kinesin-related protein XlEg5. *J Biol Chem* 274: 15005–15013

Goldenring JR (2013) A central role for vesicle trafficking in epithelial neoplasia: intracellular highways to carcinogenesis. *Nat Rev Cancer* 13: 813–820

Goldenring JR, Shen KR, Vaughan HD, Modlin IM (1993) Identification of a small GTP-binding protein, Rab25, expressed in the gastrointestinal mucosa, kidney, and lung. *J Biol Chem* 268: 18419–18422

Goldenring JR, Smith J, Vaughan HD, Cameron P, Hawkins W, Navarre J (1996) Rab11 is an apically located small GTP-binding protein in epithelial tissues. *Am J Physiol* 270: G515–G525

Goswami S, Balasubramanian I, D'Agostino L, Bandyopadhyay S, Patel R, Avasthi S, Yu S, Goldenring JR, Bonder EM, Gao N (2021) RAB11A-mediated

YAP localization to adherens and tight junctions is essential for colonic epithelial integrity. *J Biol Chem* 297: 100848

Green EG, Ramm E, Riley NM, Spiro DJ, Goldenring JR, Wessling-Resnick M (1997) Rab11 is associated with transferrin-containing recycling compartments in K562 cells. *Biochem Biophys Res Commun* 239: 612–616

Guadagno NA, Progida C (2019) Rab GTPases: switching to human diseases. *Cell* 8: 909

Hales CM, Griner R, Hobdy-Henderson KC, Dorn MC, Hardy D, Kumar R, Navarre J, Chan EK, Lapierre LA, Goldenring JR (2001) Identification and characterization of a family of Rab11-interacting proteins. *J Biol Chem* 276: 39067–39075

Hales CM, Vaerman JP, Goldenring JR (2002) Rab11 family interacting protein 2 associates with myosin Vb and regulates plasma membrane recycling. *J Biol Chem* 277: 50415–50421

Hammer JA 3rd, Wu XS (2002) Rabs grab motors: defining the connections between Rab GTPases and motor proteins. *Curr Opin Cell Biol* 14: 69–75

Hehnly H, Doxsey S (2014) Rab11 endosomes contribute to mitotic spindle organization and orientation. *Dev Cell* 28: 497–507

Hobdy-Henderson KC, Hales CM, Lapierre LA, Cheney RE, Goldenring JR (2003) Dynamics of the apical plasma membrane recycling system during cell division. *Traffic* 4: 681–693

Horgan CP, McCaffrey MW (2011) Rab GTPases and microtubule motors. *Biochem Soc Trans* 39: 1202–1206

Jiang H, He X, Wang S, Jia J, Wan Y, Wang Y, Zeng R, Yates J 3rd, Zhu X, Zheng Y (2014) A microtubule-associated zinc finger protein, BuGZ, regulates mitotic chromosome alignment by ensuring Bub3 stability and kinetochore targeting. *Dev Cell* 28: 268–281

Jin M, Goldenring JR (2006) The Rab11-FIP1/RCP gene codes for multiple protein transcripts related to the plasma membrane recycling system. *Biochim Biophys Acta* 1759: 281–295

Kajiho H, Kajiho Y, Frittoli E, Confalonieri S, Bertalot G, Viale G, Di Fiore PP, Oldani A, Garre M, Beznoussenko GV *et al* (2016) RAB2A controls MT1-MMP endocytic and E-cadherin polarized Golgi trafficking to promote invasive breast cancer programs. *EMBO Rep* 17: 1061–1080

Kashina AS, Baskin RJ, Cole DG, Wedaman KP, Saxton WM, Scholey JM (1996) A bipolar kinesin. *Nature* 379: 270–272

Kashina AS, Rogers GC, Scholey JM (1997) The bimC family of kinesins: essential bipolar mitotic motors driving centrosome separation. *Biochim Biophys Acta* 1357: 257–271

Kearney AM, Khan AR (2020) Crystal structure of the Rab-binding domain of Rab11 family-interacting protein 2. *Acta Crystallogr F Struct Biol Commun* 76: 357–363

Kelly EE, Horgan CP, McCaffrey MW (2012) Rab11 proteins in health and disease. *Biochem Soc Trans* 40: 1360–1367

Kikuchi A, Yamashita T, Kawata M, Yamamoto K, Ikeda K, Tanimoto T, Takai Y (1988) Purification and characterization of a novel GTP-binding protein with a molecular weight of 24,000 from bovine brain membranes. *J Biol Chem* 263: 2897–2904

Knowles BC, Weis VG, Yu S, Roland JT, Williams JA, Alvarado GS, Lapierre LA, Shub MD, Gao N, Goldenring JR (2015) Rab11a regulates syntaxin 3 localization and microvillus assembly in enterocytes. *J Cell Sci* 128: 1617–1626

Komarova YA, Akhmanova AS, Kojima S, Galjart N, Borisy GG (2002) Cytoplasmic linker proteins promote microtubule rescue *in vivo*. *J Cell Biol* 159: 589–599

Kumar AP, Lukman S (2018) Allosteric binding sites in Rab11 for potential drug candidates. *PLoS ONE* 13: e0198632

Lai F, Stubbs L, Artzt K (1994) Molecular analysis of mouse Rab11b: a new type of mammalian YPT/Rab protein. *Genomics* 22: 610–616

Lall P, Lindsay AJ, Hanscom S, Kecman T, Taglauer ES, McVeigh UM, Franklin E, McCaffrey MW, Khan AR (2015) Structure-function analyses of the interactions between Rab11 and Rab14 small GTPases with their shared effector Rab coupling protein (RCP). *J Biol Chem* 290: 18817–18832

Lapierre LA, Kumar R, Hales CM, Navarre J, Bhartur SG, Burnette JO, Provance DW Jr, Mercer JA, Bahler M, Goldenring JR (2001) Myosin vb is associated with plasma membrane recycling systems. *Mol Biol Cell* 12: 1843–1857

Lapierre LA, Dorn MC, Zimmerman CF, Navarre J, Burnette JO, Goldenring JR (2003) Rab11b resides in a vesicular compartment distinct from Rab11a in parietal cells and other epithelial cells. *Exp Cell Res* 290: 322–331

Li G, Marlin MC (2015) Rab family of GTPases. *Methods Mol Biol* 1298: 1–15

Lopes CS, Sampaio P, Williams B, Goldberg M, Sunkel CE (2005) The *Drosophila* Bub3 protein is required for the mitotic checkpoint and for normal accumulation of cyclins during G2 and early stages of mitosis. *J Cell Sci* 118: 187–198

Lu MS, Johnston CA (2013) Molecular pathways regulating mitotic spindle orientation in animal cells. *Development* 140: 1843–1856

Madison BB, Dunbar L, Qiao XT, Braunstein K, Braunstein E, Gumucio DL (2002) Cis elements of the villin gene control expression in restricted domains of the vertical (crypt) and horizontal (duodenum, cecum) axes of the intestine. *J Biol Chem* 277: 33275–33283

el Marjou F, Janssen KP, Chang BH, Li M, Hindie V, Chan L, Louvard D, Chambon P, Metzger D, Robine S (2004) Tissue-specific and inducible Cre-mediated recombination in the gut epithelium. *Genesis* 39: 186–193

Martinez O, Goud B (1998) Rab proteins. *Biochim Biophys Acta Mol Cell Res* 1404: 101–112

Maxfield FR, McGraw TE (2004) Endocytic recycling. *Nat Rev Mol Cell Biol* 5: 121–132

Mayer TU, Kapoor TM, Haggarty SJ, King RW, Schreiber SL, Mitchison TJ (1999) Small molecule inhibitor of mitotic spindle bipolarity identified in a phenotype-based screen. *Science* 286: 971–974

Muthu M, Cheriyan VT, Rishi AK (2015) CARP-1/CCAR1: a biphasic regulator of cancer cell growth and apoptosis. *Oncotarget* 6: 6499–6510

Nedvetsky PI, Stefan E, Frische S, Santamaria K, Wiesner B, Valenti G, Hammer JA 3rd, Nielsen S, Goldenring JR, Rosenthal W *et al* (2007) A role of myosin Vb and Rab11-FIP2 in the aquaporin-2 shuttle. *Traffic* 8: 110–123

Niwa S, Tanaka Y, Hirokawa N (2008) KIF1Bbeta- and KIF1A-mediated axonal transport of presynaptic regulator Rab3 occurs in a GTP-dependent manner through DENN/MADD. *Nat Cell Biol* 10: 1269–1279

Pierre P, Scheel J, Rickard JE, Kreis TE (1992) CLIP-170 links endocytic vesicles to microtubules. *Cell* 70: 887–900

Radulescu AE, Mukherjee S, Shields D (2011) The Golgi protein p115 associates with gamma-tubulin and plays a role in Golgi structure and mitosis progression. *J Biol Chem* 286: 21915–21926

Sakurada K, Uchida K, Yamaguchi K, Aisaka K, Ito S, Ohmori T, Takeyama Y, Ueda T, Hori Y, Ohyanagi H *et al* (1991) Molecular cloning and characterization of a ras p21-like GTP-binding protein (24KG) from rat liver. *Biochem Biophys Res Commun* 177: 1224–1232

Sato T, Clevers H (2013) Primary mouse small intestinal epithelial cell cultures. *Methods Mol Biol* 945: 319–328

Schafer JC, Baetz NW, Lapierre LA, McRae RE, Roland JT, Goldenring JR (2014) Rab11-FIP2 interaction with MYO5B regulates movement of Rab11a-containing recycling vesicles. *Traffic* 15: 292–308

Schuh M (2011) An Actin-dependent mechanism for long-range vesicle transport. *Nat Cell Biol* 13: 1431–1436

Sharp DJ, McDonald KL, Brown HM, Matthies HJ, Walczak C, Vale RD, Mitchison TJ, Scholey JM (1999) The bipolar kinesin, KLP61F, cross-links microtubules within interpolar microtubule bundles of drosophila embryonic mitotic spindles. *J Cell Biol* 144: 125–138

Shen Z, Stanger BZ (2015) YAP regulates S-phase entry in endothelial cells. *PLoS ONE* 10: e0117522

Shiba T, Koga H, Shin HW, Kawasaki M, Kato R, Nakayama K, Wakatsuki S (2006) Structural basis for Rab11-dependent membrane recruitment of a family of Rab11-interacting protein 3 (FIP3)/Arfophilin-1. *Proc Natl Acad Sci USA* 103: 15416–15421

Silvis MR, Bertrand CA, Ameen N, Golin-Bisello F, Butterworth MB, Frizzell RA, Bradbury NA (2009) Rab11b regulates the apical recycling of the cystic fibrosis transmembrane conductance regulator in polarized intestinal epithelial cells. *Mol Biol Cell* 20: 2337–2350

Skoufias DA, DeBonis S, Saoudi Y, Lebeau L, Crevel I, Cross R, Wade RH, Hackney D, Kozielski F (2006) S-trityl-L-cysteine is a reversible, tight binding inhibitor of the human kinesin Eg5 that specifically blocks mitotic progression. *J Biol Chem* 281: 17559–17569

Sobajima T, Yoshimura S, Iwano T, Kunii M, Watanabe M, Atik N, Mushiake S, Morii E, Koyama Y, Miyoshi E *et al* (2014) Rab11a is required for apical protein localisation in the intestine. *Biol Open* 4: 86–94

Starr DA, Williams BC, Li Z, Etemad-Moghadam B, Dawe RK, Goldberg ML (1997) Conservation of the centromere/kinetochore protein ZW10. *J Cell Biol* 138: 1289–1301

Subramanian A, Tamayo P, Mootha VK, Mukherjee S, Ebert BL, Gillette MA, Paulovich A, Pomeroy SL, Golub TR, Lander ES *et al* (2005) Gene set enrichment analysis: a knowledge-based approach for interpreting genome-wide expression profiles. *Proc Natl Acad Sci USA* 102: 15545–15550

Tcherniuk S, van Lis R, Kozielski F, Skoufias DA (2010) Mutations in the human kinesin Eg5 that confer resistance to monastrol and S-trityl-L-cysteine in tumor derived cell lines. *Biochem Pharmacol* 79: 864–872

Truett GE, Heeger P, Mynatt RL, Truett AA, Walker JA, Warman ML (2000) Preparation of PCR-quality mouse genomic DNA with hot sodium hydroxide and tris (HotSHOT). *Biotechniques* 29: 54

Ullrich O, Reinsch S, Urbe S, Zerial M, Parton RG (1996) Rab11 regulates recycling through the pericentriolar recycling endosome. *J Cell Biol* 135: 913–924

Vallee RB, Varma D, Dujardin DL (2006) ZW10 function in mitotic checkpoint control, dynein targeting and membrane trafficking: is dynein the unifying theme? *Cell Cycle* 5: 2447–2451

Venere M, Horbinski C, Crish JF, Jin X, Vasanji A, Major J, Burrows AC, Chang C, Prokop J, Wu Q *et al* (2015) The mitotic kinesin KIF11 is a driver of invasion, proliferation, and self-renewal in glioblastoma. *Sci Transl Med* 7: 304ra143

Wang X, Kumar R, Navarre J, Casanova JE, Goldenring JR (2000) Regulation of vesicle trafficking in madin-Darby canine kidney cells by Rab11a and Rab25. *J Biol Chem* 275: 29138–29146

Wang Z, Edwards JG, Riley N, Provance DW Jr, Karcher R, Li XD, Davison IG, Ikebe M, Mercer JA, Kauer JA *et al* (2008) Myosin Vb mobilizes recycling endosomes and AMPA receptors for postsynaptic plasticity. *Cell* 135: 535–548

Wang H, Yang H, Shivalila CS, Dawlaty MM, Cheng AW, Zhang F, Jaenisch R (2013a) One-step generation of mice carrying mutations in multiple genes by CRISPR/Cas-mediated genome engineering. *Cell* 153: 910–918

Wang L, Shi S, Guo Z, Zhang X, Han S, Yang A, Wen W, Zhu Q (2013b) Overexpression of YAP and TAZ is an independent predictor of prognosis

in colorectal cancer and related to the proliferation and metastasis of colon cancer cells. *PLoS ONE* 8: e65539

Wang K, Okada H, Bi E (2020) Comparative analysis of the roles of non-muscle myosin-IIs in cytokinesis in budding yeast, fission yeast, and mammalian cells. *Front Cell Dev Biol* 8: 593400

Wei J, Fain S, Harrison C, Feig LA, Baleja JD (2006) Molecular dissection of Rab11 binding from coiled-coil formation in the Rab11-FIP2 C-terminal domain. *Biochemistry* 45: 6826–6834

Welz T, Wellbourne-Wood J, Kerkhoff E (2014) Orchestration of cell surface proteins by Rab11. *Trends Cell Biol* 24: 407–415

Williams BC, Li Z, Liu S, Williams EV, Leung G, Yen TJ, Goldberg ML (2003) Zwilch, a new component of the ZW10/ROD complex required for kinetochore functions. *Mol Biol Cell* 14: 1379–1391

Wilson GM, Fielding AB, Simon GC, Yu X, Andrews PD, Hames RS, Frey AM, Peden AA, Gould GW, Prekeris R (2005) The FIP3-Rab11 protein complex regulates recycling endosome targeting to the cleavage furrow during late cytokinesis. *Mol Biol Cell* 16: 849–860

Wu W, Jingbo S, Xu W, Liu J, Huang Y, Sheng Q, Lv Z (2018) S-trityl-L-cysteine, a novel Eg5 inhibitor, is a potent chemotherapeutic strategy in neuroblastoma. *Oncol Lett* 16: 1023–1030

Xu S, Edman M, Kothawala MS, Sun G, Chiang L, Mircheff A, Zhu L, Okamoto C, Hamm-Alvarez S (2011) A Rab11a-enriched subapical membrane compartment regulates a cytoskeleton-dependent transcytotic pathway in secretory epithelial cells of the lacrimal gland. *J Cell Sci* 124: 3503–3514

Yang H, Wang H, Jaenisch R (2014) Generating genetically modified mice using CRISPR/Cas-mediated genome engineering. *Nat Protoc* 9: 1956–1968

Yokoyama H, Sawada JI, Sato K, Ogo N, Kamei N, Ishikawa Y, Hara K, Asai A, Hashimoto H (2018) Structural and thermodynamic basis of the enhanced interaction between kinesin spindle protein Eg5 and STLC-type inhibitors. *ACS Omega* 3: 12284–12294

Yu S, Nie Y, Knowles B, Sakamori R, Stypulkowski E, Patel C, Das S, Douard V, Ferraris RP, Bonder EM *et al* (2014a) TLR sorting by Rab11 endosomes maintains intestinal epithelial-microbial homeostasis. *EMBO J* 33: 1882–1895

Yu S, Yehia G, Wang J, Stypulkowski E, Sakamori R, Jiang P, Hernandez-Enriquez B, Tran TS, Bonder EM, Guo W *et al* (2014b) Global ablation of the mouse Rab11a gene impairs early embryogenesis and matrix metalloproteinase secretion. *J Biol Chem* 289: 32030–32043

Zhang B, Liu JF, Xu Y, Ng SC (2008a) Crystal structure of HsEg5 in complex with clinical candidate CK0238273 provides insight into inhibitory mechanism, potency, and specificity. *Biochem Biophys Res Commun* 372: 565–570

Zhang H, Squirrell JM, White JG (2008b) RAB-11 permissively regulates spindle alignment by modulating metaphase microtubule dynamics in Caenorhabditis elegans early embryos. *Mol Biol Cell* 19: 2553–2565

Zulkefli KL, Houghton FJ, Gosavi P, Gleeson PA (2019) A role for Rab11 in the homeostasis of the endosome-lysosomal pathway. *Exp Cell Res* 380: 55–68